Multiscale modeling of twinning and detwinning behavior of HCP polycrystals

Mohammadreza Yaghoobi [a,*], John E. Allison [a], Veera Sundararaghavan [b]

[a] *Materials Science and Engineering, University of Michigan, Ann Arbor, MI, 48109, USA*
[b] *Aerospace Engineering, University of Michigan, Ann Arbor, MI, 48109, USA*

ARTICLE INFO

ABSTRACT

A multiscale scheme is presented here to capture the twinning and detwinning mechanisms during cyclic loading of HCP polycrystals. In the current framework, the crystal plasticity finite element (CPFE) method is employed at the microstructural scale. The response of twinned regions at a material point is calculated using a novel homogenization scheme via a Taylor-type model. The homogenized behavior is then used in the CPFE to obtain the response of a polycrystal. An efficient rate-independent crystal plasticity model that has been incorporated into the open source *PRISMS-Plasticity* software is introduced here to capture the response of the twinned region. Accordingly, the corresponding algorithmic tangent modulus is derived. This multiscale scheme is validated against data available for the cyclic response of Mg alloy ZK60A. The results show that the multiscale model can capture the key elements of the sample response observed during the experiment.

1. Introduction

Slip and twinning are the two major deformation mechanisms of hexagonal close packed (HCP) metals. In the case of Mg alloys, basal <a> slip and extension twinning are the dominant deformation mechanisms (Begum et al., 2009; Beyerlein et al., 2010; Mirza et al., 2013; Mokdad and Chen, 2015; Yu et al., 2015). Basal slip cannot be activated during the deformation along the c-axis, and twinning becomes the dominant plasticity mechanism. Extension twinning is the most common mechanism in Mg alloys in the case of tensile loading along the c-axis (Knezevic et al., 2010; Wu et al., 2008b, 2010). The extension twin mechanism is frequently activated in wrought Mg alloys due to compression loading parallel to the basal plane which leads to the 86.3° reorientation of the basal pole. During subsequent reversed cyclic loading, i.e., tensile loading parallel to the basal plane, the size of twinned regions shrink and in some cases the twin fully disappears, a phenomenon commonly known as detwinning (Koike et al., 2010; Murphy-Leonard et al., 2019; Wu et al., 2010, 2012; Yu et al., 2011; Zhang et al., 2011, 2019). This twinning and detwinning occurs alternately during the cyclic loading of HCP samples.

To accelerate predictive materials science for design of new alloys, an integrated design framework (Aagesen et al., 2018) involving integration of experiments and multi-scale simulations has been developed within the PRISMS Center to link prediction of microstructural features of metals and alloys with predictions of their mechanical behavior. The open-source, massively parallel 3-D crystal plasticity finite element (CPFE) software package *PRISMS-Plasticity* (Yaghoobi et al., 2019) plays an important role in this integrated

---

framework. Magnesium (Mg) and its alloys serve as a prototype material system for demonstrating the capability of the PRISMS framework and the scientific advances it enables. In the case of Mg and Mg alloys, both twinning and detwinning mechanisms must be incorporated in the CPFE software to accurately capture the cyclic response of HCP metals.

Several models have been introduced to capture twinning deformation in HCP metals as well as slip due to dislocation motion (Van Houtte, 1978; Tomé et al., 1991; Kalidindi, 1998; Staroselsky and Anand, 1998, 2003; Abdolvand et al., 2011; Fernández et al., 2011, 2013; Zhang and Joshi, 2012; Liu and Wei, 2014). CPFE is one of the most common frameworks to capture twinning in HCP poly-crystals. In the case of CPFE simulation of twinning, most of the presented studies have followed two frameworks introduced by Staroselsky and Anand (1998) and Kalidindi (1998). Staroselsky and Anand (1998) incorporated the twinning into a rate-independent constitutive model. This approach has been widely incorporated to address the twinning in pure Mg and its alloys (see, e.g., Fernández et al., 2011; Fernández et al., 2013; Liu and Wei, 2014). Kalidindi (1998) modified the rate-dependent constitutive model by incorporating twinning into the plastic velocity gradient tensor. Abdolvand and his coworkers (Abdolvand et al., 2011, 2015; Abdolvand and Daymond, 2012, 2013) developed a CPFE framework which incorporates twinning by following the model proposed by Kalidindi (1998). Zhang and Joshi (2012) followed the work of Kalidindi (1998) and proposed a CPFE model with twinning which can capture the twin and slip evolution along with their interaction using a physically based model. Besides these CPFE models to capture twinning, Ardeljan et al. (2015) presented a CPFE framework which explicitly introduces the twin lamellae. Qiao et al. (2016) developed a CPFE framework which can capture the stress relaxation effect for twinning. They incorporated the stress relaxation effect for twinning, which was proposed by Wu et al. (2015) and incorporated into the elastic viscoplastic self-consistent (EVPSC) polycrystal scheme developed by Wang et al. (2010b). Hama et al. (2016) captured the anisotropic response of Mg alloy sheets during two-step loading using the CPFE framework which includes twinning. Prasad et al. (2017) incorporated twinning model into the plane strain CPFE framework to model the ductile fracture in pure Mg.

In addition to the CPFE framework, other methods have been developed to capture twinning in HCP metals. Lebensohn and Tomé (1993) incorporated twinning into the viscoplastic self-consistent (VPSC) framework to capture the texture evolution in zirconium alloys. In the case of Mg and its alloys, Agnew et al. (2001) captured the texture evolution by using the VPSC along with twinning model. The VPSC framework have been widely used to capture twinning in HCP polycrystals (see, e.g., Wang et al., 2010a; Oppedal et al., 2013; Ostapovets et al., 2013; Kabirian et al., 2015). Beyerlein and Tomé (2010) incorporated a basic probabilistic theory for the twin nucleation into the VPSC framework to capture the response of pure zirconium. They addressed the stress relaxation due to twinning by considering different critical resolved shear stresses for twin nucleation and growth. Kumar et al. (2015) incorporated twinning into a full-field elasto-viscoplastic formulation based on fast Fourier transformation. They used this model to capture the distribution of the local stress state inside the twinned domain and its neighborhood in Mg. Lévesque et al. (2016) addressed the twinning in AM30 and AZ31B Mg alloys by incorporating a twinning model into a Taylor-type crystal plasticity framework. In this model, the twinned region and untwinned parent are allowed to rotate independently. The VPSC-FE multiscale method has been developed and used to capture both twinning and slip inside polycrystals (see, e.g., Segurado et al., 2012; Knezevic et al., 2013; Prakash et al., 2015). In VPSC-FE multiscale framework, the behavior of each finite element (FE) integration point is described by a polycrystals RVE, which is homogenized by VPSC method. Ardeljan et al. (2016) and Feather et al. (2019) developed a multiscale model to capture the behavior of Mg alloys in which the upper bound Taylor-type crystal plasticity handles the meso-scale response and the FE governs the macro scale response. Kondo et al. (2014) and Liu et al. (2018) coupled a dislocation density-based crystal plasticity model with a phase field method to capture twinning in HCP metals. The phase field model governs the twin nucleation, propagation, and growth while the crystal plasticity model handle the evolutions of stress, strain, and dislocation inside the sample. Paramatmuni and Kanjarla (2019) incorporated an infinitesimal-strain crystal plasticity FFT framework to capture the twinning behavior in AZ31 Mg alloy.

While many studies have addressed twinning in HCP polycrystals, only few of these models can capture both twinning and detwinning mechanisms. Proust et al. (2007, 2009) implemented a meso-scale composite grain (CG) model in a visco-plastic self-consistent (VPSC) code which can capture both twinning and detwinning mechanisms. In this model, the manner in which twin nucleation and propagation are treated is primarily empirical in nature. Guillemer et al. (2011) implemented a simple phenomenological detwinning model into a self-consistent model to capture the cyclic behavior of extruded magnesium. Wang and his coworkers (Wang et al., 2012, 2013a, 2013b) introduced a physically based Twinning–Detwinning (TDT) model to capture both mechanisms in HCP metals. They implemented the new Twinning–Detwinning model in an EVPSC polycrystal scheme. Qiao et al. (2015) also used this TDT/EVPSC framework to capture the cyclic behavior of Mg alloy ZK60A. Twin nucleation can be readily dealt with in VPSC and EVPSC models by adding new grains. In addition, twin growth or shrinkage can be handled by varying the sizes of the parent grain, which is the twin-free part of the grain, and the newly introduced twins as children of this parent grain. Such self-consistent models are suitable for simulating the average response of a material. However, in order to handle general boundary conditions, grain distributions, adding defects such as voids, and for capturing local fields such as stress and strain, these self-consistent methods are inappropriate. One way to address these limitations is to use crystal plasticity finite element (CPFE) methods. Hama and Takuda (2012), Hama et al. (2013, 2017), Briffod et al. (2019), and Zhang et al. (2019) employed the CPFE method to model the cyclic behavior of Mg alloys. Unlike the TDT model which has a precise microstructural mechanism, Hama and Takuda (2012), Hama et al. (2013, 2017), Briffod et al. (2019), and Zhang et al. (2019) have defined the detwinning by modifying the crystal plasticity twin models using phenomenological modifications. The first challenge is that the conventional crystal plasticity constitutive models which are incorporated within the CPFEM framework to capture the twinning-detwinning mechanism (Hama and Takuda, 2012; Hama et al., 2017; Zhang et al., 2019; Briffod et al., 2019) cannot predict the reorientation of multiple twin variants at a material point and algorithms to reorient and propagate these multiple twin variants are not well developed. In these models, the material point is commonly reoriented with respect to the most active twinning system, which is commonly called the predominant twinning

reorientation (PTR) scheme (Tomé et al., 1991). The second challenge arises due to the fact that twins by themselves also deform via slip and detwinning, and the current models used within the CPFE framework cannot address these twin deformation mechanisms effectively. In other words, the stress inside the twinned region which drives these mechanisms, is different from the stress of the twin-free region. However, this is ignored in the previous CPFE simulations that have investigated the twinning-detwinning mechanisms.

In the current work, a multiscale CPFE framework is developed to address the aforementioned issues using a physically-based Twinning–Detwinning (TDT) model. The difference between the framework presented by Wang and his coworkers (Wang et al., 2012, 2013a, 2013b) and current formulation is that Wang and his coworkers (Wang et al., 2012, 2013a, 2013b) implemented the TDT model into the EVPSC polycrystal scheme. Accordingly, the twinning/detwinning mechanisms such as the growth and shrinkage of untwinned region and twin nucleation and its growth and shrinkage can be easily handled by changing the weight of the untwinned region orientation, introducing the twinned grain orientation, and varying the weight of the twinned grain orientation. Although the EVPSC polycrystal scheme is very powerful to capture the homogenized response, it cannot provide the local fields of stress and strain inside the grain. Also, it cannot handle general boundary conditions in a straight forward manner. The CPFE framework, on the other hand, can address these issues using the capabilities and features of the FE method. However, a TDT model cannot be directly implemented into the CPFE framework. The untwinned region cannot easily grow or shrink, and the new twinned grain cannot be easily introduced, grow, or shrink. In the current multiscale model, the twinning/detwinning mechanism is considered within a subscale model, where it is possible for the untwinned region and all twin variants to coexist at a material point under Taylor-type constraints. The homogenized response is then passed into the CPFE calculation. In the case of the twinning mechanism modeling, Abdolvand and Daymond (2012) proposed an uncoupled method in which the total strain increment is similar for both parent and child. Next, they calculated the stress and rotation increments for parent and child separately. Their framework is essentially an extended Taylor model to capture the twinning mechanism. In the current work, the incorporated homogenization scheme is in line with the uncoupled framework presented by Abdolvand and Daymond (2012). However, both twinning and detwinning mechanisms are considered here to capture the cyclic behavior of HCP polycrystals. In the context of modeling both twinning and detwinning mechanisms, the idea of the untwinned region and all twin variants to coexist, shrink, or grow at a material point in CPFE using a multi-level homogenization scheme has not been previously proposed, to the best of our knowledge. The model is implemented in the open-source PRISMS-Plasticity CPFE software package and will be made available as open-source software via GitHub repository (see Appendix A). A rate-independent single crystal plasticity theory is developed here to handle the response of a material point with the twinned region. An algorithmic tangent modulus is developed to numerically integrate the multiscale CPFE model. Finally, the reliability of this new framework is demonstrated by modeling the cyclic response of Mg alloy ZK60A which compares well with the experimental results of Wu (2009), Wu et al. (2008a), and Wu et al. (2008b). The results show that the multiscale model can capture both twinning and detwinning mechanisms during cyclic loadings.

2. Crystal plasticity model

A rate-independent single crystal plasticity theory is developed here to capture the behavior of twinned regions. The schematic of a material point that is twinned is depicted in Fig. 1. In the current multiscale *PRISMS-Plasticity* framework, a material point that includes a twinned region is homogenized using the Taylor model. Accordingly, both parent, i.e., twin-free or matrix region, and child, i. e., twinned region, are subjected to the same deformation gradient tensor $\mathbf{F}$. In the current formulation, the superscript mt corresponds to the parent, and the superscript tw,k corresponds to the child nucleated due to the activation of κth twin system of the parent. The subscript k denotes the child nucleated due to the activation of κth twin system of the parent. In the current model, the twinning systems are considered as pseudo-slip systems (see, e.g., Van Houtte, 1978; Staroselsky and Anand, 2003). The finite deformation continuum mechanics framework is adopted here. In the case of a material point that is twinned, a multiplicative decomposition of the
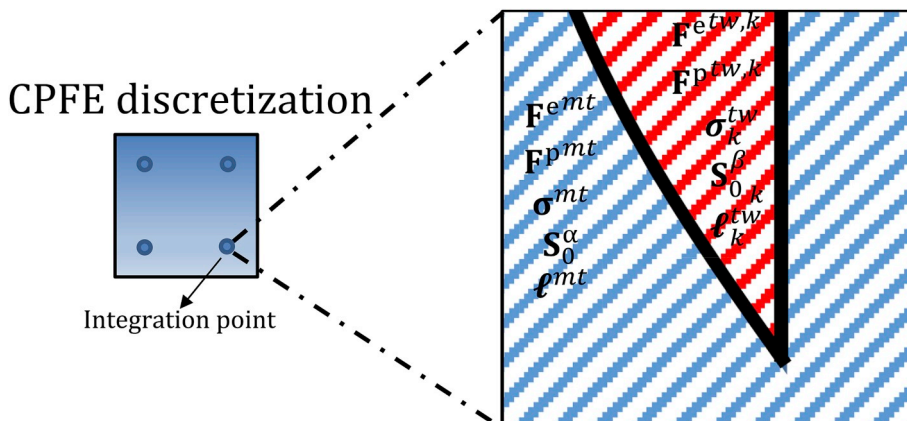

Fig. 1. The schematic of a material point with a twin. The response of the material point is homogenized using Taylor model.

deformation gradient tensor $\mathbf{F}$ into its elastic and plastic components, i.e., $\mathbf{F}^e$ and $\mathbf{F}^p$, is considered here as follows:

$$\mathbf{F} = \mathbf{F}^{e^{mt}}\mathbf{F}^{p^{mt}} = \mathbf{F}^{e^{tw,k}}\mathbf{F}^{p^{tw,k}} \tag{1}$$

In the current crystal plasticity framework, two independent deformation mechanisms of elastic distortion of the crystal lattice and pure shear as a result of plastic slip accommodate the applied deformation. In the case of a material point that is twinned, the macroscopic velocity gradient tensor $\mathbf{L}$ can be additively decomposed into the elastic and plastic components, i.e., $\mathbf{L}^e$ and $\mathbf{L}^p$, respectively, as follows:

$$\mathbf{L} = \mathbf{L}^{e^{mt}} + \mathbf{L}^{p^{mt}} = \mathbf{L}^{e^{tw,k}} + \mathbf{L}^{p^{tw,k}} \tag{2}$$

The key idea of crystal plasticity is to link the plastic part of the velocity gradient, as a representative of macroscopic response, to the superposition of shear deformation induced by crystallographic slip on multiple slip, as microscopic mechanisms of deformation, which can be described as follows:

$$\mathbf{L}^{p^{mt}} = \sum_{\alpha=1}^{N_s^{mt}+N_t^{mt}} \dot{\gamma}^{\alpha}\mathbf{S}^{\alpha}\,\mathrm{sign}(\tau^{\alpha}) \tag{3a}$$

$$\mathbf{L}^{p^{tw,k}} = \sum_{\beta=1}^{N_s^{tw}+N_t^{tw}} \dot{\tilde{\gamma}}_{\kappa}^{\beta}\mathbf{S}_k^{\beta}\,\mathrm{sign}\big(\tau_k^{\beta}\big) \tag{3b}$$

where τ^{α} and τ_k^{β} are the resolved shear stresses for slip systems α and β in parent and child, respectively. $\dot{\gamma}^{\alpha}$ is the shearing rate on α^{th} system of the parent. $\dot{\tilde{\gamma}}_{\kappa}^{\beta}$ is the shearing rate on β^{th} system of the child, which is nucleated due to the activation of κth twin system of the parent. N_s^{mt} and N_t^{mt} are the number of slip and twinning systems of a parent, respectively. In the parent grain, N_t^{mt} includes the twinning systems which govern both twin shrinkage and growth. N_t^{mt} can be considered twice the material twin systems in which the first set corresponds to the twin growth and the second set correspond to the shrinkage, which will be elaborated in the next section. For example, in the case of Mg alloys with 6 extension twinning systems of extension twin ($\{10\bar{1}2\}\langle\bar{1}011\rangle$), N_t^{mt} is 12. N_s^{tw} and N_t^{tw} are the number of slip and twinning pseudo-slip systems of child, respectively. In the child region, $N_t^{tw} = 2$ which include one growth and one shrinkage of twinned region. This twin system of the child is equivalent to the twinning system of parent which generates that child. $\mathbf{S}^{\alpha}$ is the Schmid tensor for the slip system α in parent, and $\mathbf{S}_k^{\beta}$ is the Schmid tensor for the slip system β in the child. $\mathbf{S}^{\alpha}$ and $\mathbf{S}_k^{\beta}$ can be defined as follows:

$$\mathbf{S}^{\alpha} = \mathbf{m}^{\alpha} \otimes \mathbf{n}^{\alpha} \tag{4a}$$

$$\mathbf{S}_k^{\beta} = \mathbf{m}_k^{\beta} \otimes \mathbf{n}_k^{\beta} \tag{4b}$$

where unit vectors $\mathbf{m}^{\alpha}$ and $\mathbf{n}^{\alpha}$ denote the slip direction and slip plane normal, respectively, for slip system α in parent, and unit vectors $\mathbf{m}_k^{\beta}$ and $\mathbf{n}_k^{\beta}$ denote the slip direction and slip plane normal, respectively, for slip system β in child nucleated due to the activation of κth twin system of the parent.

The resolved shear stresses in parent and child can be obtained as follows:

$$\tau^{\alpha} = \boldsymbol{\sigma}^{mt} : \mathbf{S}^{\alpha} \tag{5a}$$

$$\tau_k^{\beta} = \boldsymbol{\sigma}_k^{tw} : \mathbf{S}_k^{\beta} \tag{5b}$$

where $\boldsymbol{\sigma}^{mt}$ and $\boldsymbol{\sigma}_k^{tw}$ are the Cauchy stress tensors corresponding to the parent and child, respectively.

In the framework of the rate-independent algorithm, the yield surface can be defined as follows:

$$g^{\alpha} = |\tau^{\alpha}| - s^{\alpha} \tag{6a}$$

$$g_k^{\beta} = \big|\tau_k^{\beta}\big| - s_k^{\beta} \tag{6b}$$

where s^{α} is the slip resistance on slip system α in the parent, and s_k^{β} is the slip resistance on slip system β in the child. For slip to take place on the slip system inside the parent, $|\tau^{\alpha}|$ must reach a critical value of s^{α}. The inactive slip systems, i.e., $\dot{\gamma}^{\alpha} = 0$, are those with $|\tau^{\alpha}| < s^{\alpha}$, or $|\tau^{\alpha}| = s^{\alpha}$ and the trial stress rate points to the inside of the yield surface. If $|\tau^{\alpha}| = s^{\alpha}$ and the trial stress rate points to the outside of the yield surface, the slip system is potentially active with $\dot{\gamma}^{\alpha} \geq 0$. The same conditions can be applied to the child considering $|\tau_k^{\beta}|$ and s_k^{β}. These conditions are the specialization of the Kuhn-Tucker consistency conditions in computational plasticity and more generally in mathematical optimization.

The evolution of slip resistance in parent and child can be obtained as follows:

$$\dot{s}^{\alpha} = \sum_{\vartheta} h^{\alpha\vartheta}\dot{\gamma}^{\vartheta} \tag{7a}$$

$$s_k^\beta = \sum_\phi h_k^{\beta\phi} \dot{\bar{\gamma}}_\kappa^\phi \tag{7b}$$

where $h^{\alpha\vartheta}$ and $h_k^{\beta\phi}$ are the hardening moduli of the parent and child, respectively. $h^{\alpha\vartheta}$ and $h_k^{\beta\phi}$ define the variations of slip resistance for slip systems α and β due to the slip rate on slip systems ϑ and ϕ, respectively. $h^{\alpha\vartheta}$ can be described as a power-law relationship considering the combined effect of work hardening and recovery as follows:

$$h^{\alpha\vartheta} = \begin{cases} h_0^\vartheta \left[1 - \dfrac{s^\vartheta}{s_s^\vartheta} \right]^{a^\vartheta} & \text{if } \alpha = \vartheta \quad \left(\text{coplanar systems} \right) \\[4mm] h_0^\vartheta q \left[1 - \dfrac{s^\vartheta}{s_s^\vartheta} \right]^{a^\vartheta} & \text{if } \alpha \neq \vartheta \end{cases} \tag{8}$$

where q is the latent hardening ratio, h_0^ϑ denotes the hardening parameter for slip system ϑ, s_s^ϑ is the slip resistance at hardening saturation for slip system ϑ, and a^ϑ is a material constant for slip system ϑ which governs the sensitivity of the hardening moduli to the slip resistance. One can define $h_k^{\beta\phi}$ using the same form as presented in Eq. (8).

The homogenized Cauchy stress tensor of the material point $\boldsymbol{\sigma}$ can be obtained as the volume average of the stresses in the parent and children, i.e., twin-free and twinned regions, as follows:

$$\boldsymbol{\sigma} = (1 - f_{tw})\boldsymbol{\sigma}^{mt} + \sum_{\kappa=1}^{n_{mt}^t} f_{tw}^\kappa \boldsymbol{\sigma}_k^{tw} \tag{9}$$

where f_{tw} is the total fraction of the reoriented children nucleated due twinning, i.e., $f_{tw} = \sum\limits_{\kappa=1}^{n_{mt}^t} f_{tw}^\kappa$, f_{tw}^κ is the volume fraction of the reoriented child nucleated due to the activation of κth twin system of the parent, and n_{mt}^t is the number of nucleated children. One should notice that Eqs. (1)–(9) considered a material point that is twinned. In the case of a material point which is not twinned, the conventional rate-independent crystal plasticity formulation is used (see, e.g., Yaghoobi et al., 2019; Greeley et al., 2019; Voyiadjis and Yaghoobi, 2019). Furthermore, the detwinning mechanism is only employed in a material point with a twinned region.

3. Twinning model

The twinning and detwinning mechanisms are modeled here similar to the TDT model developed by Wang et al. (2012). Fig. 2 presents a schematic of twinning and detwinning mechanisms in a material point. Fig. 2 (a) shows a twin-free material point, which is called the parent. In Fig. 2 (b), after $f_{tw}^{\kappa*}$, i.e., the volume fraction of the child corresponding to the twin system κ of parent, reaches a critical value of f_0, a child is nucleated by lattice reorientation of parent according to the κth twin system. The twin can grow due to the parent reduction which occurs when $\tau^{N_s^{mt}+k} > s^{N_s^{mt}+k}$. The twin nucleation and growth due to parent reduction is called *operation A*. Fig. 2 (c) shows the *operation B* in which the twin grows due to the child propagation, which is activated when $\tau_k^{N_s^{tw}+2} < 0$ and $\left| \tau_k^{N_s^{tw}+2} \right| > s_k^{N_s^{tw}+2}$. The *operation C* is shown in Fig. 2 (d), which is the twin shrinkage due to the parent propagation, which occurs when $\tau^{N_s^{mt}+k+6} < 0$ and $\left| \tau^{N_s^{mt}+k+6} \right| > s^{N_s^{mt}+k+6}$. Finally, Fig. 2 (e) shows the *operation D* in which the volume of child decreases due to detwinning, which is activated when $\tau_k^{N_s^{tw}+1} > s_k^{N_s^{tw}+1}$. One should note that the conventional polarity of twinning models states that only positive resolved shear stress of twinning systems can activate twinning mechanism. Here, the polarity is modified based on the introduced TDT twinning operations (Wang et al., 2012). In the cases of *operations A and D*, positive resolved shear stresses can induce shear rates, while in the cases of *operations B and C*, negative resolved shear stresses induce shear rates.
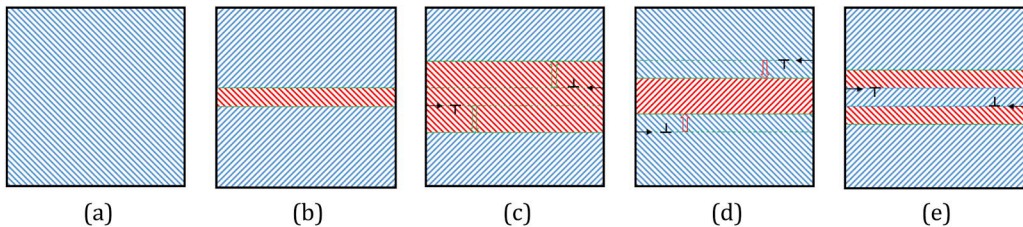

(a)   (b)   (c)   (d)   (e)

Fig. 2. The schematic of the twinning and detwinning mechanisms in a material point: (a) The material point is initially twin-free, which is called the parent (b) *Operation A:* The twin nucleation occurs when the twin volume reaches a critical value of f_0. The nucleated twin can grow due to the parent reduction. (c) *Operation B:* The twin grows due to the child propagation. (d) *Operation C:* The twin shrinks due to the parent propagation. (e) *Operation D:* The twin volume decreases due to detwinning inside the child.

Considering the four described operations, the twin volume fraction evolution of the κth twin system can be described as follows:

$$\dot{f}_{tw}^{\kappa*} = [1 - f_{tw}]\frac{(\dot{\gamma}^{N_{mt}^s+\kappa} - \dot{\gamma}^{N_{mt}^s+\kappa+6})}{S} - f_{tw}^{\kappa}\frac{(\dot{\gamma}_{\kappa}^{N_{tw}^s+1} - \dot{\gamma}_{\kappa}^{N_{tw}^s+2})}{S} \tag{10}$$

where S is the characteristic twin shear strain, which is calculated as 0.129 in the case of magnesium (Christian and Mahajan, 1995), $\dot{\gamma}^{N_{mt}^s+\kappa}$ is the shear rate of $(N_{mt}^s + \kappa)^{th}$ system inside the parent corresponds to *operation A*, $\dot{\gamma}^{N_{mt}^s+\kappa+6}$ is the shear rate of $(N_{mt}^s + \kappa + 6)^{th}$ system inside the parent corresponds to *operation C*, and $\dot{\gamma}_{\kappa}^{N_{tw}^s+1}$ and $\dot{\gamma}_{\kappa}^{N_{tw}^s+2}$ are the shear rates of $(N_{tw}^s + 1)^{th}$ and $(N_{tw}^s + 2)^{th}$ systems inside the child nucleated due to the activation of κth twin system of the parent, which corresponds to *operations B and D*, respectively. In this model, after the volume fraction of $f_{tw}^{\kappa*}$ reaches a critical value of f_0, the child is created by lattice reorientation of parent according to the κth twin system, and $\dot{f}_{tw}^{\kappa}$ and f_{tw}^{κ} become equal to $\dot{f}_{tw}^{\kappa*}$ and $f_{tw}^{\kappa*}$. Furthermore, in the case of twin shrinkage or detwinning, if f_{tw}^{κ} becomes smaller than f_0, the corresponding child will be fully detwinned. In other words, the κth child will be reoriented back to the parent grain.

The rotation matrix for rotating the crystal frame about the twin plane $\mathbf{R}_2$ can be obtained as below:

$$\mathbf{R}_2 = 2\mathbf{n}^k \otimes \mathbf{n}^k - \mathbf{I} \tag{11}$$

where $\mathbf{n}^k$ is the unit vector normal of the κth twin system, and $\mathbf{I}$ is the second order identity tensor. Also, twinning can be described an operation of rotation in which the twinned region is obtained from the untwinned one by means of rotation of π about an axis parallel to $\mathbf{n}^k$. Accordingly, the quaternion representation of twinning operation can be described as follows:

$$\mathbf{q}_{tw} = \cos\frac{\pi}{2} + \left(n_x^k\boldsymbol{i} + n_y^k\boldsymbol{j} + n_z^k\boldsymbol{k}\right)\sin\frac{\pi}{2} = \left[0, n_x^k, n_y^k, n_z^k\right] \tag{12}$$

Two schemes can be used to find the new orientation for the twinned grain. First, one can use Eq. (11) to obtain the Rodrigues vector of the twinned grain using the following procedure:

- Calculation of the rotation matrix for reference frame to crystal frame, i.e., $\mathbf{R}_1$.
- Calculation of the rotation matrix for rotating the crystal frame about the twin plane by 180°, i.e., $\mathbf{R}_2$, using Eq. (11).
- Calculation of the new rotation matrix $\mathbf{Q}$ is defined as a combination of both rotations $\mathbf{R}_2$ and $\mathbf{R}_1$ as $\mathbf{Q} = \mathbf{R}_1\mathbf{R}_2$.
- Projection of $\mathbf{Q}$ to the fundamental region, i.e., $\mathbf{QF}$, based on crystal symmetries.
- Conversion of the rotation matrix $\mathbf{QF}$ to its Rodrigues vector representation.

In the next method, one can use Eq. (12) to describe the twinning operation and obtain the Rodrigues vector of the twinned grain using the following procedure:

- Calculation of the quaternion representation of twinning operation, i.e., $\mathbf{q}_{tw}$, using Eq. (12).
- Calculation of the quaternion representation of rotation from reference frame to crystal frame, i.e., $\mathbf{q}_1$.
- Calculation of the quaternion representation of rotation from reference frame to the twinned crystal frame, i.e., $\mathbf{q}_2$, as the quaternion product of $\mathbf{q}_1$ and $\mathbf{q}_{tw}$.
- Conversion of the quaternion representation $\mathbf{q}_2$ to its Rodrigues vector representation.

It is worth mentioning that the reorientation during detwinning follows a similar formulation as twinning, which is described here.

In the current scheme, as a child is nucleated in a material point, the starting elastic and plastic deformation gradient tensors of the child are set equal to those of the parent at the time of nucleation.

The evolution of total nucleated children volume fraction f_{tw} can be defined as follows:

$$\dot{f}_{tw} = \sum_{\kappa=1}^{n_{mt}^t}\dot{f}_{tw}^{\kappa} \tag{13}$$

where n_{mt}^t is the number of children nucleated due to twinning with a twin volume fraction larger than f_0. Three more constants can be defined to generalize this twin model. First, the total twin volume fraction f_{tw} cannot exceed the empirical constant of f_{max}. In other words, twinning of a material point stops as soon as f_{tw} reaches f_{max}, and other mechanisms will govern the plastic deformation. A second constant is defined that represents the maximum allowed twinning volume fraction inside each grain, i.e., f_{max}^{grain}. Accordingly, when f_{tw} in a particular grain reaches f_{max}^{grain}, the grain cannot undergo additional twinning. Lastly, one can define a critical value of $f_{max}^{critical}$ such that when a material point with twin volume f_{tw}^{κ} reaches $f_{max}^{critical}$, the material point is reoriented according to the κth twin system.

It is worth mentioning that the simple twinning-detwinning models incorporated in Hama and Takuda (2012), Hama et al. (2017), Briffod et al. (2019), and Zhang et al. (2019) can be obtained as a special case of the general TDT model presented here. By considering $f_0 = f_{max}^{critical}$, a simple phenomenological twinning-detwinning model can be obtained in a way that there are only two conditions for a material point; it either consists of parent grain or it becomes reoriented according to the dominant twin variant. Accordingly, if one is

not interested in using the general framework of *PRISMS-Plasticity* TDT model, the model can be reduced to a phenomenological twinning-detwinning simulation by calibrating $f_0 = f_{max}^{critical}$ (see, e.g., Briffod et al., 2019).

4. Incremental formulation

An incremental scheme is incorporated to numerically solve the equilibrium equation of the body in which the deformed body at time $= t$ with the observable thermodynamics variables of $\{\mathbf{F}(t),\ \mathbf{F}^{\mathrm{e}^{mt}}(t),\ \mathbf{F}^{\mathrm{p}^{mt}}(t), \mathbf{F}^{\mathrm{e}^{tw,k}}(t), \mathbf{F}^{\mathrm{p}^{tw,k}}(t), \boldsymbol{\sigma}^{mt}(t), \sigma_k^{tw}(t), f_{tw}^{\kappa}(t), s^{\alpha}(t), s_k^{\beta}(t)\}$ undergoes the incremental deformation and the new deformed body at time $\tau = t + \Delta t$ has the updated observable thermodynamics variables of $\{\mathbf{F}(\tau),\ \mathbf{F}^{\mathrm{e}^{mt}}(\tau),\ \mathbf{F}^{\mathrm{p}^{mt}}(\tau),\ \mathbf{F}^{\mathrm{e}^{tw,k}}(\tau),\ \mathbf{F}^{\mathrm{p}^{tw,k}}(\tau),\ \boldsymbol{\sigma}^{mt}(\tau),\ \sigma_k^{tw}(\tau),\ f_{tw}^{\kappa}(\tau),\ s^{\alpha}(\tau), s_k^{\beta}(\tau)\}$. The constitutive law can be described as below:

$$\mathbf{S}^{mt}(\tau) = \boldsymbol{\ell}^{mt}[\mathbf{E}^{\mathrm{e}mt}(\tau)] \tag{14a}$$

$$\mathbf{S}_k^{tw}(\tau) = \boldsymbol{\ell}_k^{tw}[\mathbf{E}^{\mathrm{e}tw,k}(\tau)] \tag{14b}$$

Where $\mathbf{S}^{mt}(\tau)$ and $\mathbf{S}_k^{tw}(\tau)$ are the second Piola-Kirchhoff (PKII) stress tensors in parent and child, respectively, relative to the relaxed configuration at time τ. $\boldsymbol{\ell}^{mt}$ and $\boldsymbol{\ell}_k^{tw}$ are the fourth order elastic stiffness tensors for parent and child, respectively. Finally, $\mathbf{E}^{\mathrm{e}mt}(\tau)$ and $\mathbf{E}^{\mathrm{e}tw,k}(\tau)$ are the elastic Green strain tensors at time τ for parent and child, respectively, which can be defined as follows:

$$\mathbf{E}^{\mathrm{e}mt}(\tau) = \frac{1}{2}[\mathbf{C}^{\mathrm{e}mt}(\tau) - \mathbf{I}] \tag{15a}$$

$$\mathbf{E}^{\mathrm{e}tw,k}(\tau) = \frac{1}{2}\left[\mathbf{C}^{\mathrm{e}tw,k}(\tau) - \mathbf{I}\right] \tag{15b}$$

where $\mathbf{I}$ is the second order identity tensor, and $\mathbf{C}^{\mathrm{e}mt}(\tau)$ and $\mathbf{C}^{\mathrm{e}tw,k}(\tau)$ are the elastic right Cauchy-Green deformation tensors at time τ for parent and child, respectively, which can be defined as follows:

$$\mathbf{C}^{\mathrm{e}mt}(\tau) = \mathbf{F}^{\mathrm{e}mt}(\tau)^{\mathrm{T}}\mathbf{F}^{\mathrm{e}mt}(\tau) \tag{16a}$$

$$\mathbf{C}^{\mathrm{e}tw,k}(\tau) = \mathbf{F}^{\mathrm{e}tw,k}(\tau)^{\mathrm{T}}\mathbf{F}^{\mathrm{e}tw,k}(\tau) \tag{16b}$$

The relation between the PKII stress tensor and the Cauchy stress tensor can be defined as follows:

$$\mathbf{S}^{mt}(\tau) = J^{\mathrm{e}mt}\mathbf{F}^{\mathrm{e}mt}(\tau)^{-1}\boldsymbol{\sigma}^{mt}(\tau)\mathbf{F}^{\mathrm{e}mt}(\tau)^{-\mathrm{T}} \tag{17a}$$

$$\mathbf{S}_k^{tw}(\tau) = J^{\mathrm{e}tw,k}\mathbf{F}^{\mathrm{e}tw,k}(\tau)^{-1}\boldsymbol{\sigma}_k^{tw}(\tau)\mathbf{F}^{\mathrm{e}tw,k}(\tau)^{-\mathrm{T}} \tag{17b}$$

where $J^{\mathrm{e}mt} = \det[\mathbf{F}^{\mathrm{e}mt}(\tau)]$ and $J^{\mathrm{e}tw,k} = \det[\mathbf{F}^{\mathrm{e}tw,k}(\tau)]$. The resolved shear stresses in parent and child can be obtained using the corresponding PKII stress tensor as follows:

$$\tau^{\alpha}(\tau) = \{\mathbf{C}^{\mathrm{e}mt}(\tau)\mathbf{S}^{mt}(\tau)\} : \mathbf{S}_0^{\alpha} \tag{18a}$$

$$\tau_k^{\beta}(\tau) = \left\{\mathbf{C}^{\mathrm{e}tw,k}(\tau)\mathbf{S}_k^{tw}(\tau)\right\} : \mathbf{S}_0^{\beta}k \tag{18b}$$

where $\mathbf{S}_0^{\alpha}$ and $\mathbf{S}_0^{\beta}k$ are the Schmid tensor for slip systems α and β in parent and child, respectively, corresponding to the relaxed configuration, which are the same as those in the undeformed configuration. In the case of infinitesimal elastic stretches, Eq. (18) can be simplified by neglecting elastic stretches as below:

$$\tau^{\alpha}(\tau) = \mathbf{S}^{mt}(\tau) : \mathbf{S}_0^{\alpha} \tag{19a}$$

$$\tau_k^{\beta}(\tau) = \mathbf{S}_k^{tw}(\tau) : \mathbf{S}_0^{\beta}k \tag{19b}$$

The trial state is defined to develop a framework of constitutive model integration, in which the incremental deformation from time $= t$ to time $= \tau$ is assumed to be purely elastic. The trial elastic deformation gradient tensors of parent and child can be obtained as follows:

$$\mathbf{F}^{\mathrm{e}mt}(\tau)^{\mathrm{tr}} = \mathbf{F}(\tau)\mathbf{F}^{\mathrm{p}mt}(t)^{-1} \tag{20a}$$

$$\mathbf{F}^{\mathrm{e}tw,k}(\tau)^{tr} = \mathbf{F}(\tau)\mathbf{F}^{\mathrm{p}tw,k}(t)^{-1} \tag{20b}$$

The trial elastic right Cauchy-Green deformation tensor and trial elastic Green strain tensor can be obtained similar to Eqs. (15) and (16). The trial PKII stress tensors of parent and child can then obtained as below:

$$\mathbf{S}^{mt}(\tau)^{\text{tr}} = \boldsymbol{\ell}^{mt}[\mathbf{E}^{\text{e}mt}(\tau)^{\text{tr}}] \tag{21a}$$

$$\mathbf{S}_k^{tw}(\tau)^{tr} = \boldsymbol{\ell}_k^{tw}[\mathbf{E}^{\text{e}tw,k}(\tau)^{tr}] \tag{21b}$$

Finally, the trial resolved shear stresses of parent and child can be described as follows:

$$\tau^{\alpha}(\tau)^{\text{tr}} = \mathbf{S}^{mt}(\tau)^{\text{tr}} : \mathbf{S}_0^{\alpha} \tag{22a}$$

$$\tau_k^{\beta}(\tau)^{tr} = \mathbf{S}_k^{tw}(\tau)^{tr} : \mathbf{S}_0^{\beta}k \tag{22b}$$

The incremental flow rule is obtained by integration of Eq. (3) followed by a linearization as follows:

$$\mathbf{F}^{\text{p}mt}(\tau) = \left[\mathbf{I} + \sum_{\alpha} \Delta\gamma^{\alpha}\text{sign}[\tau^{\alpha}(\tau)^{\text{tr}}]\mathbf{S}_0^{\alpha}\right]\mathbf{F}^{\text{p}mt}(t) \tag{23a}$$

$$\mathbf{F}^{\text{p}tw,k}(\tau) = \left[\mathbf{I} + \sum_{\beta} \Delta\overline{\gamma}_{\kappa}^{\beta}\text{sign}[\tau_k^{\beta}(\tau)^{tr}]\mathbf{S}_{0_k}^{\beta}\right]\mathbf{F}^{\text{p}tw,k}(t) \tag{23b}$$

In the case of the trial resolved shear stress point inside the yield surface, the slip system is inactive and the corresponding shearing rate is zero. However, the slip system can be potentially active if the trial resolve shear stress point located outside of the yield surface. The final active systems are the slip systems with the shearing increment larger than zero, i.e., $\Delta\gamma^{\alpha} > 0$ in parent and $\Delta\overline{\gamma}_{\kappa}^{\beta} > 0$ in child, which should be among the potential active ones. Finally, the slip resistances in parent and child are updated using the obtained shearing increments as follows:

$$s^{\alpha}(\tau) = s^{\alpha}(t) + \sum_{\vartheta \in \mathscr{A}} h^{\alpha\vartheta}(t)\Delta\gamma^{\vartheta} \tag{24a}$$

$$s_k^{\beta}(\tau) = s_k^{\beta}(t) + \sum_{\phi \in \mathscr{A}_k} h^{\beta\phi}(t)\Delta\overline{\gamma}_{\kappa}^{\phi} \tag{24b}$$

where $\mathscr{A}$ and $\mathscr{A}_k$ represents the set of active slip systems in parent and child, respectively.

The elastic deformation gradient tensor $\mathbf{F}^{\text{e}}(\tau)$ can be obtained using Eq. (23) by neglecting the higher order terms of shearing increment as follows:

$$\mathbf{F}^{\text{e}mt}(\tau) = \mathbf{F}^{\text{e}mt}(\tau)^{\text{tr}}\left[\mathbf{I} - \sum_{\alpha} \Delta\gamma^{\alpha}\text{sign}[\tau^{\alpha}(\tau)^{\text{tr}}]\mathbf{S}_0^{\alpha}\right] \tag{25a}$$

$$\mathbf{F}^{\text{e}tw,k}(\tau) = \mathbf{F}^{\text{e}tw,k}(\tau)^{\text{tr}}\left[\mathbf{I} - \sum_{\beta} \Delta\overline{\gamma}_{\kappa}^{\beta}\text{sign}[\tau_k^{\beta}(\tau)^{tr}]\mathbf{S}_{0_k}^{\beta}\right] \tag{25b}$$

Accordingly, the PKII stress tensor at time $= \tau$ can be obtained as follows:

$$\mathbf{S}^{mt}(\tau) = \mathbf{S}^{mt}(\tau)^{\text{tr}} - \sum_{\alpha \in \mathscr{A}} \Delta\gamma^{\alpha}\text{sign}[\tau^{\alpha}(\tau)^{\text{tr}}]\boldsymbol{\ell}^{mt}\left[\text{sym}(\mathbf{C}^{\text{e}mt}(\tau)^{\text{tr}}\mathbf{S}_0^{\alpha})\right] \tag{26a}$$

$$\mathbf{S}_k^{tw}(\tau) = \mathbf{S}_k^{tw}(\tau)^{\text{tr}} - \sum_{\beta \in \mathscr{A}_k} \Delta\overline{\gamma}_{\kappa}^{\beta}\text{sign}[\tau_k^{\beta}(\tau)^{tr}]\boldsymbol{\ell}_k^{tw}\left[\text{sym}(\mathbf{C}^{\text{e}tw,k}(\tau)^{\text{tr}}\mathbf{S}_{0_k}^{\beta})\right] \tag{26b}$$

The resolved shear stress at time $= \tau$ can then be obtained as follows:

$$|\tau^{\alpha}(\tau)| = |\tau^{\alpha}(\tau)^{\text{tr}}| - \sum_{\vartheta \in \mathscr{A}} \text{sign}[\tau^{\alpha}(\tau)^{\text{tr}}]\text{sign}[\tau^{\vartheta}(\tau)^{\text{tr}}]\mathbf{S}_0^{\alpha} : \boldsymbol{\ell}^{mt}\left[\text{sym}(\mathbf{C}^{\text{e}mt}(\tau)^{\text{tr}}\mathbf{S}_0^{\vartheta})\right]\Delta\gamma^{\vartheta} \tag{27a}$$

$$\left|\tau_k^{\beta}(\tau)\right| = \left|\tau_k^{\beta}(\tau)^{tr}\right| - \sum_{\phi \in \mathscr{A}_k} sign\left[\tau_k^{\beta}(\tau)^{tr}\right]\text{sign}[\tau_k^{\phi}(\tau)^{tr}]\mathbf{S}_{0_k}^{\beta} : \boldsymbol{\ell}_k^{tw}\left[sym(\mathbf{C}^{\text{e}tw,k}(\tau)^{tr}\mathbf{S}_{0_k}^{\phi})\right]\Delta\gamma^{\phi} \tag{27b}$$

The consistency condition, i.e., Eq. (6), can be rewritten by incorporating Eqs. (24) and (27) as follows:

$$\sum_{\vartheta \in \mathscr{A}} A^{\alpha\vartheta}x^{\vartheta} = b^{\alpha} \tag{28a}$$

$$\sum_{\phi \in \mathscr{A}_k} A^{\beta\phi}x^{\phi} = b^{\beta} \tag{28b}$$

where:

$$A^{\alpha\vartheta} = h^{\alpha\vartheta}(t) + \text{sign}[\tau^{\alpha}(\tau)^{\text{tr}}]\text{sign}[\tau^{\vartheta}(\tau)^{\text{tr}}]\mathbf{S}_0^{\alpha} : \boldsymbol{\ell}^{mt}\left[\text{sym}(\mathbf{C}^{\text{e}mt}(\tau)^{\text{tr}}\mathbf{S}_0^{\vartheta})\right] \tag{29}$$

$$b^\alpha = |\tau^\alpha(\tau)^{\text{tr}}| - s^\alpha(t) > 0 \tag{30}$$

$$x^\vartheta = \Delta\gamma^\vartheta \tag{31}$$

$$A^{\beta\phi} = h^{\beta\phi}(t) + sign[\tau_k^\beta(\tau)^{tr}] sign[\tau_k^\phi(\tau)^{tr}] \mathbf{S}_0^\beta k : \boldsymbol{\ell}_k^{tw} \left[sym \left(\mathbf{C}^{etw,k}(\tau)^{tr} \mathbf{S}_0^\phi k \right) \right] \tag{32}$$

$$b^\beta = |\tau_k^\beta(\tau)^{tr}| - s_k^\beta(t) > 0 \tag{33}$$

$$x^\phi = \Delta\overline{\gamma}_\kappa^\phi \tag{34}$$

After solving Eqs. (28a) and (29-31) for parent and Eqs. (28b) and (32-34) for child, the slip systems with $x^\vartheta = \Delta\gamma^\vartheta \leq 0$ and $x^\phi = \Delta\overline{\gamma}_\kappa^\phi \leq 0$ should be removed from the active slip system set. Accordingly, Eqs. (28-34) should be updated and solved again until all active slip systems have $\Delta\gamma > 0$. After obtaining the consistent set of values for $\Delta\gamma$ for each active slip system, the plastic deformation gradient is updated using Eq. (23). It is noted that Eq. (23) does not ensure that $\det[\mathbf{F}^{p mt}(\tau)] = 1$ and $\det[\mathbf{F}^{p tw,k}(\tau)] = 1$. Accordingly, one should normalize the plastic deformation gradient tensors of both parent and child. Next, the elastic deformation gradient is updated using the multiplicative decomposition as described in Eq. (1). The PKII stress tensor is then obtained using Eq. (14), and the updated Cauchy stress tensor is obtained as below:

$$\boldsymbol{\sigma}^{mt}(\tau) = J^{e-1} \mathbf{F}^{emt}(\tau) \mathbf{S}^{mt}(\tau) \mathbf{F}^{emt}(\tau)^{\text{T}} \tag{35a}$$

$$\boldsymbol{\sigma}_k^{tw}(\tau) = J^{etw,k-1} \mathbf{F}^{etw,k}(\tau) \mathbf{S}_k^{tw}(\tau) \mathbf{F}^{etw,k}(\tau)^{\text{T}} \tag{35b}$$

Finally, the slip resistances can then be updated by using Eq. (24).

After updating the constitutive model of parent and children, the volume fraction of the child, which is nucleated due to the activation of κth twin system of the parent, at time $= \tau$, i.e., $f_{tw}^\kappa(\tau)$, can be obtained using Eq. (10) as follows:

$$f_{tw}^{\kappa*}(\tau) = f_{tw}^{\kappa*}(t) + [1 - f_{tw}(t)] \frac{(\Delta\gamma^{N_{mt}^s+\kappa} - \Delta\gamma^{N_{mt}^s+\kappa+6})}{S} - f_{tw}^\kappa(t) \frac{(\Delta\overline{\gamma}_\kappa^{N_{tw}^s+1} - \Delta\overline{\gamma}_\kappa^{N_{tw}^s+2})}{S} \tag{36}$$

After the volume fraction of $f_{tw}^{\kappa*}$ reaches a critical value of f_0, the child is created by lattice reorientation of parent according to the κth twin system, and $\dot{f}_{tw}^\kappa$ and f_{tw}^κ become equal to $\dot{f}_{tw}^{\kappa*}$ and $f_{tw}^{\kappa*}$.

The total fraction of the reoriented children nucleated due twinning at time $= \tau$, i.e., $f_{tw}(\tau)$, can be obtained as follows:

$$f_{tw}(\tau) = \sum_{\kappa=1}^{n_{mt}^t} f_{tw}^\kappa(\tau) \tag{37}$$

where n_{mt}^t is the number of child nucleated due to twinning.

The homogenized Cauchy stress tensor of the material point can be obtained as the volume average of the stresses in the parent and children as follows:

$$\boldsymbol{\sigma}(\tau) = [1 - f_{tw}(\tau)] \boldsymbol{\sigma}^{mt}(\tau) + \sum_{\kappa=1}^{n_{mt}^t} f_{tw}^\kappa(\tau) \boldsymbol{\sigma}_k^{tw}(\tau) \tag{38}$$

The last step is to develop the algorithmic tangent modulus, which is described in the next section.

5. Algorithmic tangent modulus

The Newton-Raphson iterative scheme with a line search procedure is employed here to solve the nonlinear system of equilibrium equation. The material tangent modulus A has a key role in this iterative scheme, which can be described as follows (Yaghoobi et al., 2019; Voyiadjis and Yaghoobi, 2019):

$$A \equiv \left. \frac{\partial \mathbf{P}}{\partial \mathbf{F}} \right|_{\mathbf{F}_n} \tag{39}$$

where $\mathbf{P}$ is the first Piola-Kirchhoff (PKI) stress tensor. The derivation of the material tangent modulus A is an important part of any implicit scheme which should be accurately calculated to solve the problem. Since the derivation of material tangent modulus A depends on the incorporated integration algorithm, it is commonly termed as the algorithmic tangent modulus.

As a first step, the homogenized PKI stress tensor $\mathbf{P}$ of a material point can be defined as the volume average of the stresses in the parent and children as follows:

$$\mathbf{P} = [1 - f_{tw}] \mathbf{P}^{mt} + \sum_{\kappa=1}^{n_{mt}^t} f_{tw}^\kappa \mathbf{P}_k^{tw} \tag{40}$$

The variation of PKI stress tensor can then be obtained as follows:

$$\delta(\mathbf{P}) = (1 - f_{tw})\delta(\mathbf{P}^{mt}) + \sum_{\kappa=1}^{n_{mt}^t} f_{tw}^{\kappa}\delta(\mathbf{P}_k^{tw}) - \delta(f_{tw})\mathbf{P}^{mt} + \sum_{\kappa=1}^{n_{mt}^t} \delta(f_{tw}^{\kappa})\mathbf{P}_k^{tw} \tag{41}$$

The relations between $\delta(\mathbf{P}^{mt})$ and $\delta(\mathbf{P}_k^{tw})$ with $\delta(\mathbf{F})$ can be obtained by following the derivation of the relation between $\delta(\mathbf{P})$ with $\delta(\mathbf{F})$ in the standard rate-independent CPFE implementation, as described in Yaghoobi et al. (2019). In the case of the relation between $\delta(\mathbf{P}^{mt})$ with $\delta(\mathbf{F})$, one should use the parent set of variables as $\{\mathbf{F}, \mathbf{F}^{e^{mt}}, \mathbf{F}^{p^{mt}}, \boldsymbol{\sigma}^{mt}, \mathbf{S}_0^{\alpha}, \boldsymbol{\ell}^{mt}, \mathbf{F}^{e^{mt^{tr}}}, \Delta\gamma^{\alpha}\}$, and in the case of the relation between $\delta(\mathbf{P}_k^{tw})$ with $\delta(\mathbf{F})$, one should use the child set of variables as $\{\mathbf{F}, \mathbf{F}^{e^{tw,k}}, \mathbf{F}^{p^{tw,k}}, \boldsymbol{\sigma}_k^{tw}, \mathbf{S}_{0_k}^{\beta}, \boldsymbol{\ell}_k^{tw}, \mathbf{F}^{e^{tw,k^{tr}}}, \Delta\overline{\gamma}_{\kappa}^{\beta}\}$.

To derive the algorithmic tangent modulus A, two more terms of $\delta(f_{tw})$ and $\delta(f_{tw}^{\kappa})$ in Eq. (41) should be related to $\delta(\mathbf{F})$. First, one can define $\delta(f_{tw})$ using Eq. (37) as follows:

$$\delta(f_{tw}) = \sum_{\kappa=1}^{n_{mt}^t} \delta(f_{tw}^{\kappa}) \tag{42}$$

Accordingly, the algorithmic tangent modulus A can be derived by obtaining $\delta(f_{tw}^{\kappa})$ as a function of $\delta(\mathbf{F})$. Here, it is assumed that $f_{tw}^{\kappa^*}$ reaches a critical value of f_0, and accordingly, $\dot{f}_{tw}^{\kappa^*}$ and $f_{tw}^{\kappa^*}$ become equal to $\dot{f}_{tw}^{\kappa^*}$ and $f_{tw}^{\kappa^*}$. To obtain $\delta(f_{tw}^{\kappa})$ as a function of $\delta(\mathbf{F})$, Eq. (36) can be used as a starting point. Accordingly, $\delta(f_{tw}^{\kappa})$ can be derived as follows:

$$\delta(f_{tw}^{\kappa}) = [1 - f_{tw}(t)]\frac{[\delta(\Delta\gamma^{N_{mt}^s+\kappa}) - \delta(\Delta\gamma^{N_{mt}^s+\kappa+6})]}{S} - f_{tw}^{\kappa}(t)\frac{[\delta(\Delta\overline{\gamma}_{\kappa}^{N_{tw}^s+1}) - \delta(\Delta\overline{\gamma}_{\kappa}^{N_{tw}^s+2})]}{S} \tag{43}$$

Note that $\delta(f_{tw}(t))$ and $\delta(f_{tw}^{\kappa}(t))$ can be approximated as zero because any variation of the deformation gradient tensor, i.e., $\delta(\mathbf{F})$, does not change the observable thermodynamics variables obtained in earlier time steps.

Now, the terms $\delta(\Delta\gamma^{N_{mt}^s+\kappa})$, $\delta(\Delta\gamma^{N_{mt}^s+\kappa+6})$, $\delta(\Delta\overline{\gamma}_{\kappa}^{N_{tw}^s+1})$, and $\delta(\Delta\overline{\gamma}_{\kappa}^{N_{tw}^s+2})$ should be defined. The first two terms belong to the parent and the last ones belong to the children. To obtain these terms, one can drop the superscripts from Eq. (28) and apply the variation operator as follows:

$$\mathbf{b} = \mathbf{A}\boldsymbol{\Delta\gamma} \rightarrow \delta\mathbf{b} = \delta\mathbf{A}\boldsymbol{\Delta\gamma} + \mathbf{A}\delta(\boldsymbol{\Delta\gamma}) \tag{44}$$

Accordingly, $\delta(\boldsymbol{\Delta\gamma})$ can be obtained as follows:

$$\delta(\boldsymbol{\Delta\gamma}) = \mathbf{A}^{-1}(\delta\mathbf{b} - \delta\mathbf{A}\boldsymbol{\Delta\gamma}) \tag{45}$$

After obtaining the $\delta(\boldsymbol{\Delta\gamma})$ vector for both parent and child, one can pick the terms $\delta(\Delta\gamma^{N_{mt}^s+\kappa})$, $\delta(\Delta\gamma^{N_{mt}^s+\kappa+6})$, $\delta(\Delta\overline{\gamma}_{\kappa}^{N_{tw}^s+1})$, and $\delta(\Delta\overline{\gamma}_{\kappa}^{N_{tw}^s+2})$. In the case of the parent, the term $\delta\mathbf{b}$ can be derived using Eq. (30) as follows:

$$\delta b^{\alpha} = \text{sign}(\tau^{\alpha^{tr}})\delta\mathbf{S}^{mt^{tr}} : \mathbf{S}_0^{\alpha} - \delta(s^{\alpha}(t)) \approx \text{sign}(\tau^{\alpha^{tr}})\boldsymbol{\ell}^{mt}[\delta(\mathbf{E}^{e^{mt^{tr}}})] : \mathbf{S}_0^{\alpha} \tag{46}$$

One can obtain $\delta\mathbf{b}$ for the child using Eq. (33) as follows:

$$\delta b^{\beta} = \text{sign}(\tau_k^{\beta^{tr}})\delta\mathbf{S}_k^{tw^{tr}} : \mathbf{S}_{0_k}^{\beta} - \delta(s_k^{\beta}(t)) \approx \text{sign}(\tau_k^{\beta^{tr}})\boldsymbol{\ell}_k^{tw}[\delta(\mathbf{E}^{e^{tw,k^{tr}}})] : \mathbf{S}_{0_k}^{\beta} \tag{47}$$

Note that in Eqs. (46) and (47), $\delta(s^{\alpha}(t))$ and $\delta(s_k^{\beta}(t))$ can be approximated as zero because any variation of the deformation gradient tensor, i.e., $\delta(\mathbf{F})$, does not change the observable thermodynamics variables obtained in earlier time steps. Following the same procedure, $\delta\mathbf{A}$ of the parent can be obtained using Eq. (29) as follows:

$$\delta A^{\alpha\vartheta} = \delta(h^{\alpha\vartheta}(t)) + \text{sign}(\tau^{\alpha^{tr}})\text{sign}(\tau^{\vartheta^{tr}})\mathbf{S}_0^{\alpha} : \boldsymbol{\ell}^{mt}[\delta(\mathbf{B}^{\vartheta^{tr}})]$$

$$\approx \text{sign}(\tau^{\alpha^{tr}})\text{sign}(\tau^{\vartheta^{tr}})\mathbf{S}_0^{\alpha} : \boldsymbol{\ell}^{mt}[\delta(\mathbf{B}^{\vartheta^{tr}})] \tag{48}$$

Where $\delta(\mathbf{B}^{\vartheta^{tr}})$ can be defined as follows:

$$\delta(\mathbf{B}^{\vartheta^{tr}}) = \frac{1}{2}\left[(\mathbf{S}_0^{\vartheta})^{\text{T}}\delta(\mathbf{C}^{e^{mt^{tr}}})^{\text{T}} + \delta(\mathbf{C}^{e^{mt^{tr}}})\mathbf{S}_0^{\vartheta}\right] = \left[(\mathbf{S}_0^{\vartheta})^{\text{T}}\delta(\mathbf{E}^{e^{mt^{tr}}})^{\text{T}} + \delta(\mathbf{E}^{e^{mt^{tr}}})\mathbf{S}_0^{\vartheta}\right] \tag{49}$$

In the case of the child, $\delta\mathbf{A}$ can be obtained using Eq. (32) as follows:

$$\delta A^{\beta\phi} = \delta(h^{\beta\phi}(t)) + \text{sign}(\tau_k^{\beta^{tr}})\text{sign}(\tau_k^{\phi^{tr}})\mathbf{S}_0^{\beta}k : \boldsymbol{\ell}_k^{tw}[\delta(\mathbf{B}_k^{\phi^{tr}})]$$

$$\approx \text{sign}(\tau_k^{\beta^{tr}})\text{sign}(\tau_k^{\phi^{tr}})\mathbf{S}_0^{\beta}k : \boldsymbol{\ell}_k^{tw}[\delta(\mathbf{B}_k^{\phi^{tr}})] \tag{50}$$

Where $\delta(\mathbf{B}_k^{\phi^{tr}})$ can be defined as follows:

$$\delta\left(\mathbf{B}_k^{\phi\,\mathrm{tr}}\right) = \frac{1}{2}\left[\left(\mathbf{S}_0^\phi k\right)^{\mathrm{T}}\delta\left(\mathbf{C}^{e\,tw,k\,\mathrm{tr}}\right)^{\mathrm{T}} + \delta\left(\mathbf{C}^{e\,tw,k\,\mathrm{tr}}\right)\mathbf{S}_0^\phi k\right] = \left[\left(\mathbf{S}_0^\phi k\right)^{\mathrm{T}}\delta\left(\mathbf{E}^{e\,tw,k\,\mathrm{tr}}\right)^{\mathrm{T}} + \delta\left(\mathbf{E}^{e\,tw,k\,\mathrm{tr}}\right)\mathbf{S}_0^\phi k\right] \tag{51}$$

One can define $\delta(\Delta\boldsymbol{\gamma})$ as a function of $\delta(\mathbf{E}^{e\,mt\,\mathrm{tr}})$ and $\delta(\mathbf{E}^{e\,tw,k\,\mathrm{tr}})$ in the parent and child, respectively, by substituting Eqs. (46-51) into Eq. (45). The rest of the derivation, which are the relations between $\delta(\mathbf{E}^{e\,mt\,\mathrm{tr}})$ and $\delta(\mathbf{E}^{e\,tw,k\,\mathrm{tr}})$ with $\delta\mathbf{F}$ are the same as the relation between $\delta(\mathbf{E}^{e\,\mathrm{tr}})$ with $\delta\mathbf{F}$ in the standard rate-independent CPFE implementation, as described in Yaghoobi et al. (2019). In the case of the relation between $\delta(\mathbf{E}^{e\,mt\,\mathrm{tr}})$ with $\delta\mathbf{F}$, one should use the parent set of variables as $\{\mathbf{F}, \mathbf{F}^{e\,mt}, \mathbf{F}^{p\,mt}, \boldsymbol{\sigma}^{mt}, \mathbf{S}_0^\alpha, \boldsymbol{\ell}^{mt}, \mathbf{F}^{e\,mt\,\mathrm{tr}}, \Delta\gamma^\alpha\}$, and in the case of the relation between $\delta(\mathbf{E}^{e\,tw,k\,\mathrm{tr}})$ with $\delta\mathbf{F}$, one should use the child set of variables as $\{\mathbf{F}, \ \mathbf{F}^{e\,tw,k}, \ \mathbf{F}^{p\,w,k}, \ \boldsymbol{\sigma}_k^{tw}, \ \mathbf{S}_{0_k}^\beta, \ \boldsymbol{\ell}_k^{tw}, \ \mathbf{F}^{e\,tw,k\,\mathrm{tr}}, \ \Delta\bar{\gamma}_\kappa^\beta\}$.

6. Results and discussion

The cyclic response of extruded Mg alloy ZK60A sample is simulated here to investigate the *PRISMS-Plasticity* TDT multiscale framework. Wu (2009), Wu et al. (2008a), and Wu et al. (2008b) investigated the cyclic stress-strain response and texture evolution of the extruded Mg alloy ZK60A sample, which is measured using synchrotron X-ray diffraction. The sample has the typical extruded sample texture with the basal poles oriented normal to the extrusion direction and the loading direction. Due to the lack of availability of the texture used by Wu and coworkers (Wu et al., 2008a, 2008b; Wu, 2009), a typical wrought Mg texture, which was used to model the extruded Mg alloy ZK60A sample (Yaghoobi et al., 2019), is used here for this analysis. Fig. 3 shows the assumed initial pole figures that were generated using MATLAB toolbox MTEX (Bachmann et al., 2010). The initial multiscale CPFE framework calibration for the uniaxial compression and tension loadings is described below. This is followed by the discussion of the simulation of the sample during cyclic response.

6.1. Multiscale CPFE framework calibration

As a starting point, the TDT model was calibrated using the experimental uniaxial responses. Three slip modes of Basal $\langle a\rangle$ ($\{0001\}\langle 11\bar{2}0\rangle$), Prismatic $\langle a\rangle$ ($\{10\bar{1}0\}\langle 11\bar{2}0\rangle$), and Pyramidal $\langle c + a\rangle$ ($\{\bar{1}\bar{1}22\}\langle\bar{1}\bar{1}23\rangle$), along one extension twin mode ($\{10\bar{1}2\}\langle\bar{1}011\rangle$) are considered to model the deformation mechanisms of a simulated ZK60A sample. The polycrystalline sample is modeled as an aggregate of 1080 single crystals (grains), which reproduces the extruded sample, each grain being modeled by a single eight-node linear hexahedral element. Accordingly, an $8 \times 9 \times 15$ FE cubic mesh is generated in the x, y, and z directions, in which each element represents a single grain. The tensile and compressive displacements are applied in the z direction, which is the extrusion direction, to mimic the uniaxial tension and compression tests, respectively. Symmetry boundary conditions are imposed on adjacent x, y, and z faces (Yaghoobi et al., 2019). The elastic constants of pure Mg at room temperature (Long and Smith, 1957; Slutsky and Garland, 1957; Zhang and Joshi, 2012) are incorporated here for the sample and are presented in Table 1. The initial critical resolved shear stresses and the hardening parameters for different slip and twin modes are calibrated to capture the uniaxial tensile and compressive loadings. Table 2 presents the initial slip resistances and corresponding hardening parameters for slip and twining modes. As described by Qiao et al. (2015), the critical resolved shear stress for *operation A* is higher than those for *operations B* and *C*. Also, similar to Qiao et al. (2015), the critical resolved shear stress for *operation D* is considered to be similar to those of *operations B* and *C*. Following Wang and his coworkers (Wang et al., 2012, 2013a, 2013b) and Qiao et al. (2015), the latent hardening parameter q is taken to be one for all deformation modes. The selection of latent hardening within hexagonal close packed is a topic of ongoing investigation, and limited research has been conducted on this topic (see e.g., Lavrentev and Pokhil, 1975; Hiura, 2010). The twinning parameters of $f_0 = 0.03$ and $f_{max}^{grain} = f_{max} = 0.65$ are selected. $f_0 = 0.03$ is calibrated using the initial phase of twinning during uniaxial compression test. $f_{max}^{grain} = f_{max} = 0.65$ is selected to accurately capture the length of the plateau and the steepness of the subsequent
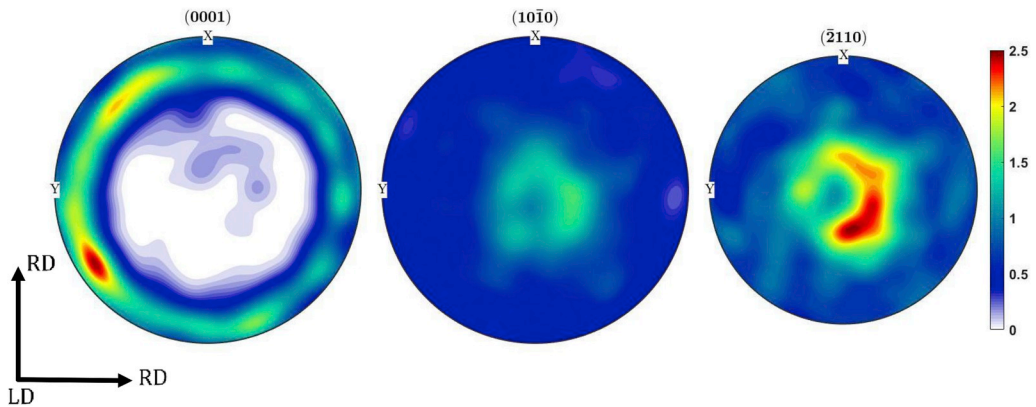

Fig. 3. Pole figures showing the initial texture of the extruded sample with the basal poles aligned perpendicular to the loading direction. LD: Loading Direction (Extrusion Direction); RD: Radial Direction (normal to the loading direction).

Table 1
The elastic constants (MPa) of pure Mg at room temperature.

C11	C12	C13	C33	C44
59,400	25,610	21,440	61,600	16,400

Table 2
The calibrated values of initial slip resistance and corresponding hardening parameters for slip and twining modes of Mg alloy ZK60A.

Mode	s_0^α (MPa)	h_0^α (MPa)	s_s^α (Mpa)	a^α
Basal	20	10	21	2
Prismatic	140	20	155	2
Pyramidal<c+a>	240	1000	350	6
Twinning (*operation A*)	48	800	52	0
Twinning (*operations B,C, D*)	15	800	25	0

strain hardening during uniaxial compression test. Fig. 4 shows the stress-strain responses of extruded Mg alloy ZK60A sample during uniaxial tension and compression loadings along the extrusion direction obtained using the multiscale CPFE simulation compared to the experimental values reported by Wu (2009). The results show that both compressive and tensile stress-strain behaviors are precisely captured using the calibrated model.

The relative activity of slip and twin modes are presented in Fig. 5. At low stresses, the dominant deformation mechanisms is basal slip. In the case of uniaxial tensile loading, as the sample begins to yield macroscopically, non-basal slip modes become increasingly active. Among these, the prismatic is the dominant non-basal mode of deformation. In the case of uniaxial compression loading, similar to the tensile loading, basal slip is the dominant deformation mode at low stresses. However, as the sample begins to macroscopically yield, the extension twinning mode becomes active and has a key role in the response of the sample. Fig. 5 also shows the variation of twin volume fraction as the strain increases during the simulated uniaxial tension and compression tests. The results show that the twin volume fraction is approximately 58%, i.e., $f_{tw} \cong 58\%$, at 12% uniaxial compressive strain, while the twin volume fraction is less than 5% in the case of 12% uniaxial tensile strain. This demonstrates the importance of the extension twinning mode in capturing the anisotropy of the extruded sample during the uniaxial loading along the extrusion direction. To further investigate the extension twinning mechanism, Fig. 6 shows the contributions of parent and children in twin volume fraction. There is no twinned region for low strains. Accordingly, the increase in twinning volume is due to the twin nucleation and growth in the parent, i.e., f_{tw}^{par}, which can be observed in Fig. 6. As the strain increases, the twinning due to twin activation inside the twinned regions, i.e., f_{tw}^{ch}, becomes considerable. A similar trend was observed by Qiao et al. (2015).
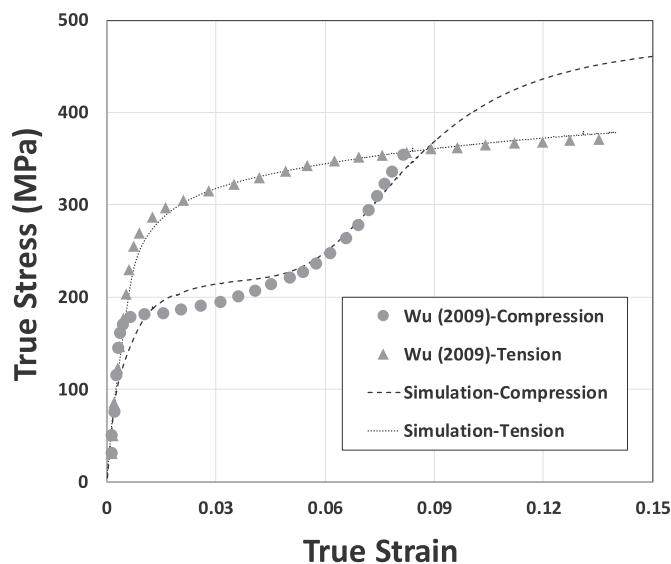

Fig. 4. The responses of Mg alloy ZK60A sample during uniaxial tension and compression loadings along the extrusion direction. The simulation results are compared with experimental values reported by Wu (2009).
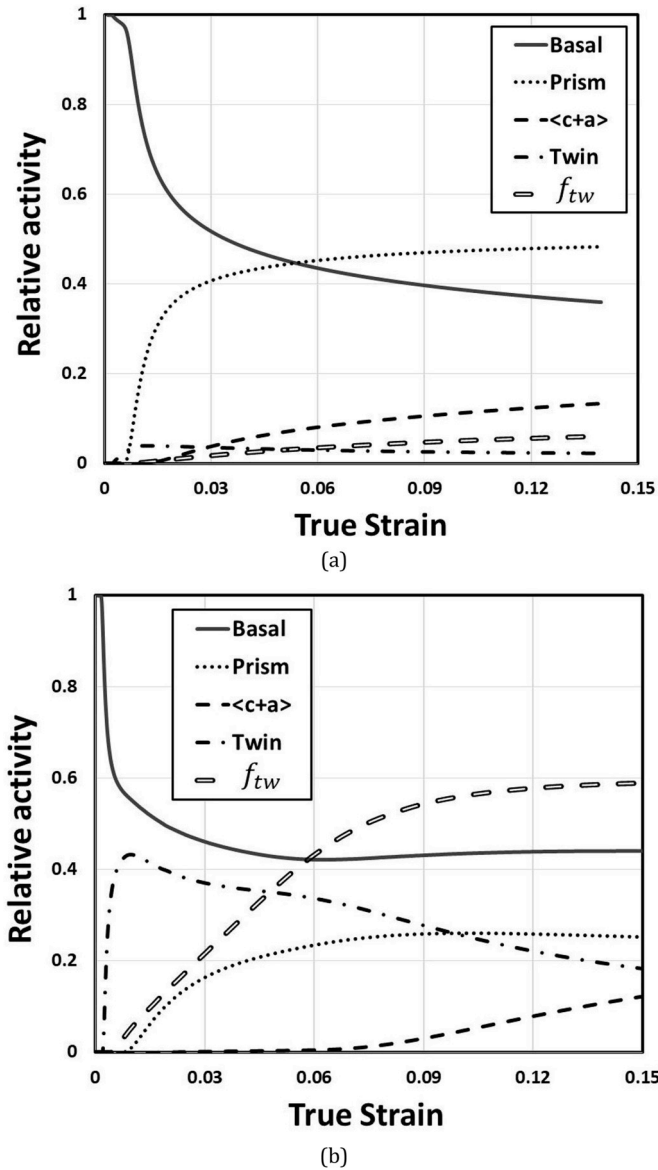
(a)

(b)

Fig. 5. The predicted relative activities of slip and twin modes of Mg alloy ZK60A sample during uniaxial loadings along the extrusion direction: (a) uniaxial tension (b) uniaxial compression. The variation of twin volume fraction f_{tw} as the true strain varies is also shown.

6.2. Cyclic response of extruded Mg alloy ZK60A

The cyclic response of the extruded Mg alloy ZK60A sample during the initial uniaxial compressive loading up to the strain of 0.012 and subsequent two full loading cycles are captured using the developed multiscale model and compared against the experimental results of Wu (2009) and Wu et al. (2008b), as shown in Fig. 7. The results show that the current model can successfully capture the cyclic response of the sample. In order to unravel the underlying deformation mechanisms during the cyclic loading, the variation of twin volume fraction during the cyclic loading should be investigated. To do so, the variation of the normalized intensity of the {0002} diffraction peak along the longitudinal direction reported by Wu et al. (2008a) can be considered. In the case of experimental results of Wu et al. (2008a), the normalized intensity of $\cong 0.22$ corresponds to the initial sample with no twinning. Furthermore, the change in the normalized intensity can be taken to be proportional to the change in the twin volume fraction (Murphy-Leonard et al., 2019). Accordingly, Fig. 8 compares the variation of the normalized intensity of the {0002} diffraction peak along the longitudinal direction reported by Wu et al. (2008a) versus the strain against the twin volume fraction variation versus the strain obtained using the multiscale CPFE simulation. The results show that the model can successfully capture the twin volume variation during the experiment. Fig. 9 shows the initial and subsequent simulated basal (0001) pole figures at strains of $\varepsilon = \pm 1.2\%$. The results show that the twinning mechanism leads to the reorientation of the basal pole and increases in the basal {0002} peak intensity in loading direction at first
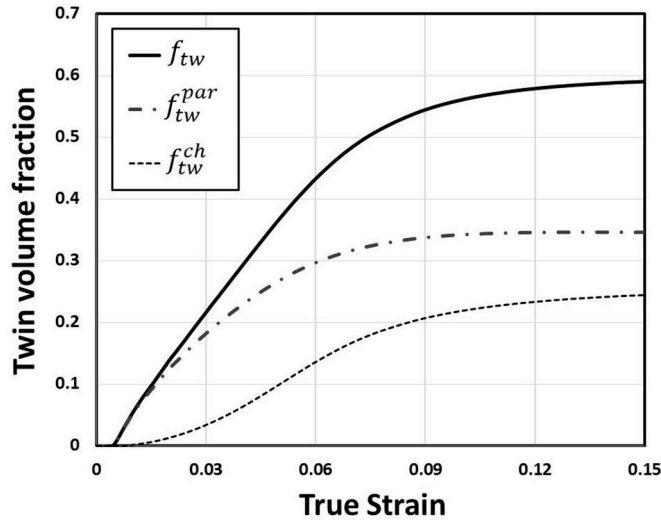
Fig. 6. Contributions of parent and children in twinning volume in a simulation of Mg alloy ZK60A sample during uniaxial compression along the extrusion direction.
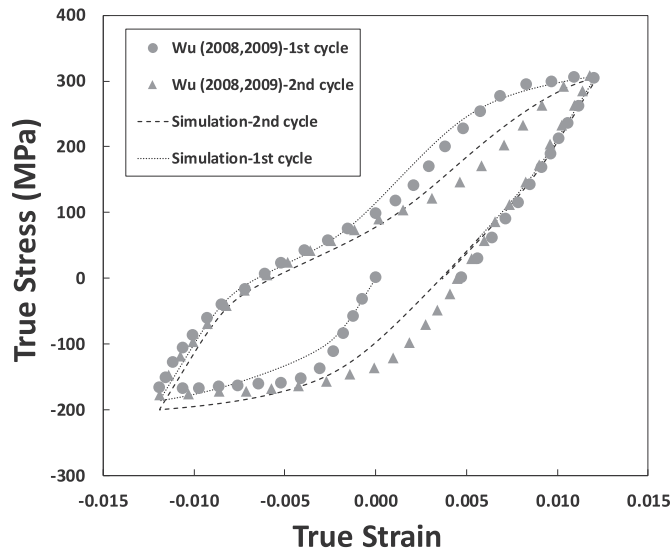

Fig. 7. Cyclic response of the extruded Mg alloy ZK60A sample along the extrusion direction. The simulation results are compared with experimental values reported by Wu et al. (2008b) and Wu (2009).

quarter of cycles 1 and 2, i.e., $\varepsilon = -1.2\%$, as shown in the center of the pole figure presented in Fig. 9(b) and (d). On the other hand, the detwinning mechanism removes the induced basal {0002} peak intensity in the loading direction during the third quarter of cycles 1 and 2, i.e., $\varepsilon = 1.2\%$, and the pole figures becomes similar to that of the initial texture, as shown in Fig. 9(c) and (e).

In order to further investigate the deformation mechanisms of the extruded Mg alloy ZK60A sample during the cyclic loading, the relative activity of the predicted slip and twin modes can be studied. Accordingly, the first cycle is divided into four stages of loading including: *Stage I. Compressive loading, Stage II. Compressive unloading, Stage III. Tensile loading*, and *Stage IV. Tensile unloading*. The relative activity of predicted slip and twinning modes are presented for all these four stages in Fig. 10. Here, the twinning and detwinning mechanisms are separated to precisely capture the governing deformation mechanisms of the sample during the cyclic loading. In the case of stage *I* of compressive loading, initially, the sample is slip free. At low strains, basal slip becomes the dominant deformation mode. As compression loading continued, eventually, the twin deformation mechanism becomes activated, and the twin volume fraction increases to around 7.5 % at the end of the *stage I*. In the case of stage *II* of compressive unloading, the response is initially elastic as predicted, and the relative activities of different deformation mechanisms do not change. Eventually, as we go closer to the uniaxial tensile loading stage, the detwinning mechanism is activated and its relative activity increases which leads to the detwinning and decrease in the total twin volume fraction. In Stage *III* and transition to the tensile loading, initially, the relative
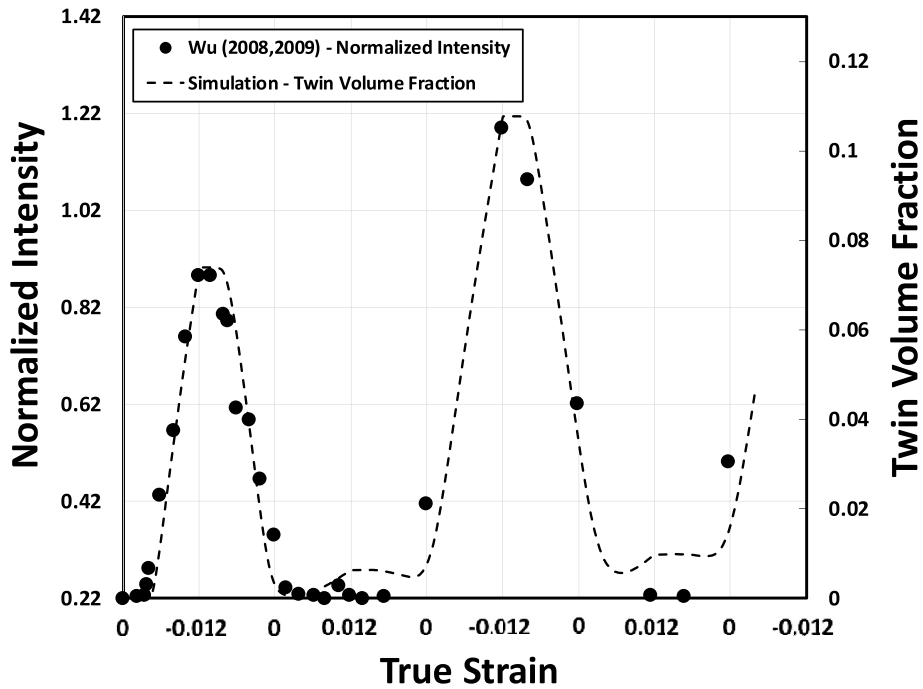
Fig. 8. Comparison of the measured variation of the normalized intensity of the {0002} diffraction peak along the longitudinal direction reported by Wu et al. (2008a) and Wu (2009) versus the twin volume fraction variation predicted using the multiscale *PRISMS-Plasticity* model during the cyclic loading of the extruded Mg alloy ZK60A sample along the extrusion direction.
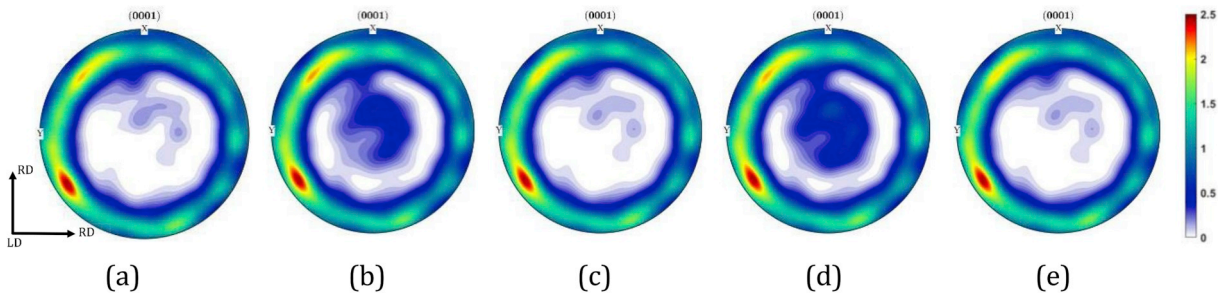

Fig. 9. The predicted basal (0001) pole figures of: (a) Initial texture (b) First quarter of cycle 1 ($\varepsilon = -1.2\%$) (c) Third quarter of cycle 1 ($\varepsilon = 1.2\%$) (d) First quarter of cycle 2 ($\varepsilon = -1.2\%$) (e) Third quarter of cycle 2 ($\varepsilon = 1.2\%$).

activity of basal slip increases slightly followed by increase in the relative activity of prismatic deformation. In the tensile unloading stage (Stage *IV*), the response is initially elastic and there is no change in the relative slip activity. Eventually, the basal deformation mechanism is the only deformation mode which is active in this region of stresses and its relative activity increases slightly.

Some key differences of the present multiscale model with traditional CPFE scheme incorporated to capture twinning and det-winning mechanisms (see, e.g., Hama and Takuda, 2012; Hama et al., 2017; Zhang et al., 2019; Briffod et al., 2019) are worth discussing. In the PTR scheme used in the CPFE modeling of twinning-detwinning simulation, when the volume fraction of a twin variant reaches a critical value, the material point is reoriented according to that variant and the other twin variants are eliminated (see, e.g., Choi et al., 2011). In the presented multiscale framework, multiple twin variants are allowed to exist at a material point in various volume fractions. Unlike the PTR scheme, the volume fractions of non-predominant twin variants are not unphysically transferred to the predominant variant. The developed treatment is similar to volume fraction transfer (VFT) schemes that track all twin variants in the orientation space. Similar to PTR scheme, this work also implements a threshold volume fraction to activate crystal reorientation when a certain volume fraction is reached. Once a twinned region is formed by reorientation according to the twin variant, the slip and detwinning mechanisms are considered inside this twinned region. No other twin variants are considered inside the twinned region to avoid the exponential complexity of formation of another twin inside the twinned region.

Another key improvement from traditional CPFE schemes, which were used to model the twinning and detwinning mechanisms, is the difference in the stress states used to achieve twinning and detwinning. Twinning and detwinning in traditional PTR schemes is based on a stress criteria that is related to the stress state of the material point. However, in the current multiscale approach, multiple
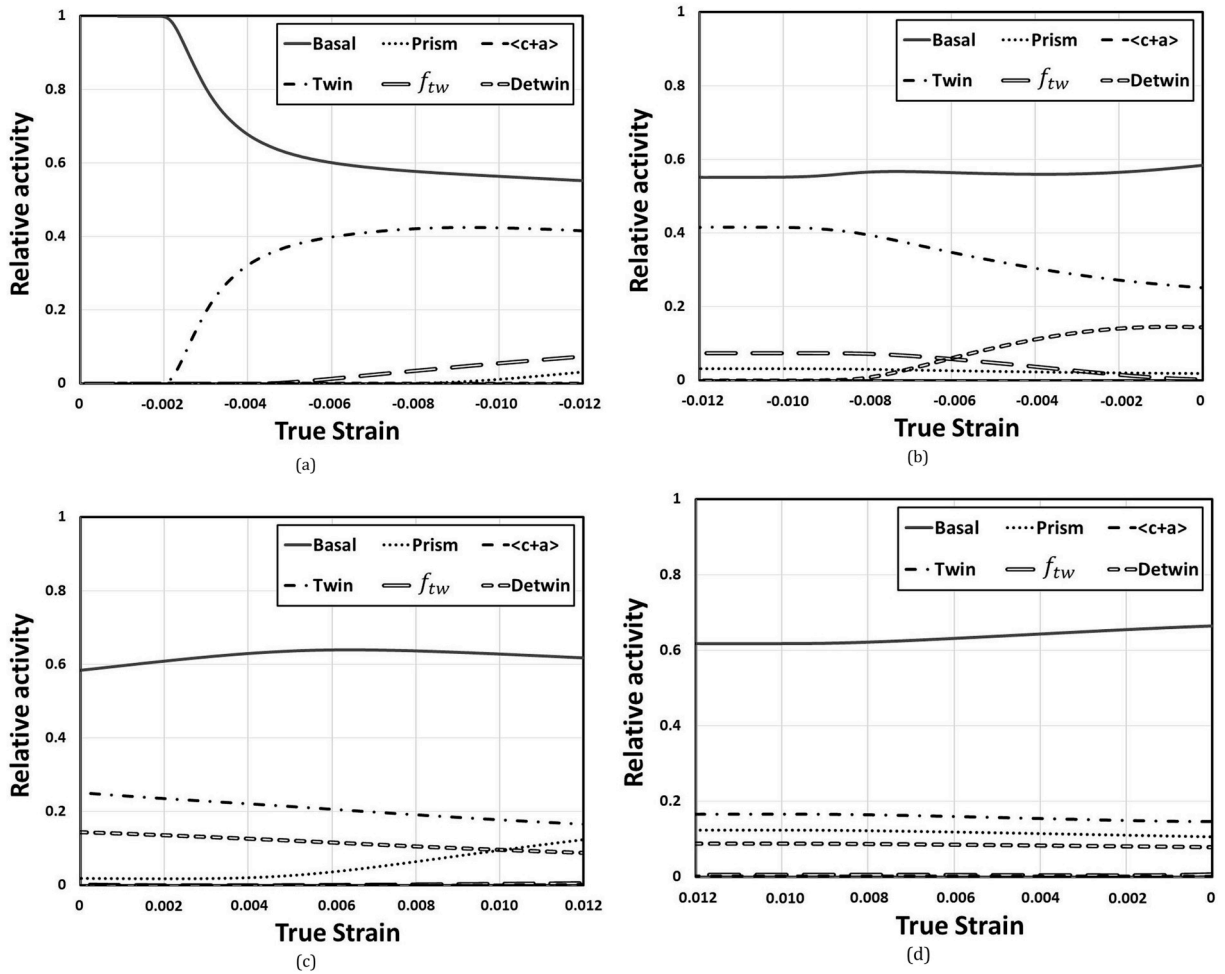
Fig. 10. The relative activities of slip and twin modes in simulation of Mg alloy ZK60A sample during cyclic loading along the extrusion direction: (a) *Stage I. Compressive loading* (b) *Stage II. Compressive unloading* (c) *Stage III. Tensile loading* (d) *Stage IV. Tensile unloading*. The variation of twin volume fraction f_{tw} as the true strain varies is also shown.

stress states are available at a material point due to the presence of parent and twinned children. This aspect is similar to the Twin-ning–DeTwinning (TDT) model presented by Wang and his coworkers (Wang et al., 2012, 2013a, 2013b) where both parent and children stress states are considered for twin volume fraction evolution in both twinning and detwinning mechanisms.

While the cyclic loading behavior of the Mg alloy is satisfactorily captured using the developed multiscale approach, several improvements can be incorporated into the model. Due to the use of finite element scheme, equilibrium at the polycrystal scale is enforced which locally captures the interaction between twins and parent across the integration points. However, at the scale of an integration point itself, the Taylor assumption is employed here that does not consider the equilibrium (and thus interactions) between the twins and slip systems. Modeling such interactions is complex due to the unknown geometries of parent and twin regions and the parent – twin interface at an integration point. One possible approach is to change the latent hardening constants to account for slip twin interactions. For example, Oppedal et al. (2012) addressed this problem by modifying the latent hardening behavior of slip within twin variants. Due to the difficulty of calibrating these additional latent hardening constants, it has been neglected in the current work. However, with increased resolution of experimental characterization techniques, improved models accounting for complex parent – twin interactions at a material point can be developed in the future which would lead to a better understanding of deformation in HCP alloys.

7. Summary

A multiscale CPFE framework is developed here to capture the twinning and detwinning mechanisms of HCP metals during cyclic loadings. Current CPFE implementations of the twinning and detwinning mechanisms have difficulties in accounting for multiple active twin variants at material points and the deformation mechanisms within these twins. The available CPFE models also do not consider the contribution of stress inside the twin itself to slip, twinning, and detwinning. The key contribution of this paper is the

incorporation of a physically-based twinning-detwinning model (TDT) model into an open-source CPFE framework. Accordingly, the response of a material point is defined using the TDT model which contains both twinned and untwinned regions of multiple variants. The response of the material point is homogenized via a Taylor-type model, which is then incorporated into the CPFE simulation to capture the response of the sample. The physically-based TDT model can capture twin nucleation, growth, and shrinkage in addition to the detwinning. The TDT model described here has been previously implemented in the EVPSC polycrystal scheme but not in a CPFE framework. The twinning-detwinning model is incorporated into a rate-independent crystal plasticity model and the corresponding algorithmic tangent modulus is derived here. The multiscale scheme is implemented in the open-source parallel 3-D crystal plasticity finite element (CPFE) software package *PRISMS-Plasticity*. The model is calibrated using the response of the extruded Mg alloy ZK60A sample during uniaxial compressive and tensile loadings along the extrusion directions. The model successfully captures the experimentally reported anisotropy of the extruded sample. Finally, the developed multiscale framework successfully captures the cyclic response of the extruded Mg alloy ZK60A sample. The results show the importance of the twinning and detwinning mechanisms of both parent grain, i.e., twin free region, and twinned children in capturing the cyclic response of the extruded Mg alloy ZK60A.

Declaration of competing interest

The authors declare that they have no known competing financial interests or personal relationships that could have appeared to influence the work reported in this paper.

The authors declare the following financial interests/personal relationships which may be considered as potential competing interests:

CRediT authorship contribution statement

Mohammadreza Yaghoobi: Conceptualization, Formal analysis, Investigation, Methodology, Supervision, Validation, Visualization, Writing - original draft, Writing - review & editing. **John E. Allison:** Conceptualization, Project administration, Methodology, Funding acquisition, Supervision, Writing - review & editing. **Veera Sundararaghavan:** Conceptualization, Project administration, Formal analysis, Investigation, Methodology, Supervision, Writing - review & editing.

Acknowledgment

Appendix A

- *PRISMS-Plasticity* software can be freely downloaded from the following link: https://github.com/prisms-center/plasticity.
- Input files for the CPFEM simulations can be downloaded from Materials Commons using the following link: https://materialscommons.org/mcapp/#/data/dataset/d9cd5ea2-224a-4830-bcf1-f69f0d923108. Also, the dataset is published for these input files at Materials Commons at https://doi.org/10.13011/m3-ae14-g783.

Appendix B. Supplementary data

Supplementary data to this article can be found online at https://doi.org/10.1016/j.ijplas.2019.102653.

References

Aagesen, L.K., Adams, J.F., Allison, et al., 2018. PRISMS: an integrated, open-source framework for accelerating predictive structural materials science. JOM 70, 2298–2314.

Abdolvand, H., Daymond, M.R., 2012. Internal strain and texture development during twinning: comparing neutron diffraction measurements with crystal plasticity finite-element approaches. Acta Mater. 60, 2240–2248.

Abdolvand, H., Daymond, M.R., 2013. Multi-scale modeling and experimental study of twin inception and propagation in hexagonal close-packed materials using a crystal plasticity finite element approach; part II: local behavior. J. Mech. Phys. Solids 61, 803–818.

Abdolvand, H., Daymond, M.R., Mareau, C., 2011. Incorporation of twinning into a crystal plasticity finite element model: evolution of lattice strains and texture in Zircaloy-2. Int. J. Plast. 27, 1721–1738.

Abdolvand, H., Majkut, M., Oddershede, J., Wright, J.P., Daymond, M.R., 2015. Study of 3-D stress development in parent and twin pairs of a hexagonal close-packed polycrystal: Part II – crystal plasticity finite element modeling. Acta Mater. 93, 235–245.

Agnew, S.R., Yoo, M.H., Tomé, C.N., 2001. Application of texture simulation to understanding mechanical behavior of Mg and solid solution alloys containing Li or Y. Acta Mater. 49, 4277–4289.

Ardeljan, M., Beyerlein, I.J., McWilliams, B.A., Knezevic, M., 2016. Strain rate and temperature sensitive multi-level crystal plasticity model for large plastic deformation behavior: application to AZ31 magnesium alloy. Int. J. Plast. 83, 90–109.

Ardeljan, M., McCabe, R.J., Beyerlein, I.J., Knezevic, M., 2015. Explicit incorporation of deformation twins into crystal plasticity finite element models. Comput. Methods Appl. Mech. Eng. 295, 396–413.

Bachmann, F., Hielscher, R., Schaeben, H., 2010. Texture analysis with MTEX – free and open source software toolbox. Solid State Phenom. 160, 63–68.

Begum, S., Chen, D.L., Xu, S., Luo, A.A., 2009. Low cycle fatigue properties of an extruded AZ31 magnesium alloy. Int. J. Fatigue 31, 726–735.

Beyerlein, I.J., Capolungo, L., Marshall, P.E., McCabe, R.J., Tome, C.N., 2010. Statistical analyses of deformation twinning in magnesium. Philos. Mag. 90, 2161–2190.

Beyerlein, I.J., Tomé, C.N., 2010. A probabilistic twin nucleation model for HCP polycrystalline metals. Proc. R. Soc. A Math. Phys. Eng. Sci. 466, 2517–2544.

Briffod, F., Shiraiwa, T., Enoki, M., 2019. Numerical investigation of the influence of twinning/detwinning on fatigue crack initiation in AZ31 magnesium alloy. Mater. Sci. Eng., A 753, 79–90.

Choi, S.H., Kim, D.W., Seong, B.S., Rollett, A.D., 2011. 3-D simulation of spatial stress distribution in an AZ31 Mg alloy sheet under in-plane compression. Int. J. Plast. 27, 1702–1720.

Christian, J.W., Mahajan, S., 1995. Deformation twinning. Prog. Mater. Sci. 39, 1–157.

Feather, W.G., Ghorbanpour, S., Savage, D.J., Ardeljan, M., Jahedi, M., McWilliams, B.A., Gupta, N., Xiang, C., Vogel, S.C., Knezevic, M., 2019. Mechanical response, twinning, and texture evolution of WE43 magnesium-rare earth alloy as a function of strain rate: experiments and multi-level crystal plasticity modeling. Int. J. Plast. 120, 180–204.

Fernández, A., Jérusalem, A., Gutiérrez-Urrutia, I., Pérez-Prado, M.T., 2013. Three-dimensional investigation of grain boundary-twin interactions in a Mg AZ31 alloy by electron backscatter diffraction and continuum modeling. Acta Mater. 61, 7679–7692.

Fernández, A., Pérez Prado, M.T., Wei, Y., Jérusalem, A., 2011. Continuum modeling of the response of a Mg alloy AZ31 rolled sheet during uniaxial deformation. Int. J. Plast. 27, 1739–1757.

Greeley, D., Yaghoobi, M., Pagan, D., Sundararaghavan, V., Allison, J., 2019. Using synchrotron radiation to improve understanding of deformation of polycrystalline metals by measuring, modelling and publishing 4D information. IOP Conf. Ser. Mater. Sci. Eng. 580, 012017.

Guillemer, C., Clavel, M., Cailletaud, G., 2011. Cyclic behavior of extruded magnesium: experimental, microstructural and numerical approach. Int. J. Plast. 27, 2068–2084.

Hama, T., Kitamura, N., Takuda, H., 2013. Effect of twinning and detwinning on inelastic behavior during unloading in a magnesium alloy sheet. Mater. Sci. Eng., A 583, 232–241.

Hama, T., Kobuki, A., Takuda, H., 2017. Crystal-plasticity finite-element analysis of anisotropic deformation behavior in a commercially pure titanium Grade 1 sheet. Int. J. Plast. 91, 77–108.

Hama, T., Takuda, H., 2012. Crystal plasticity finite-element simulation of deformation behavior in a magnesium alloy sheet considering detwinning. In: Steel Research International SPL. ISSUE, pp. 1115–1118.

Hama, T., Tanaka, Y., Uratani, M., Takuda, H., 2016. Deformation behavior upon two-step loading in a magnesium alloy sheet. Int. J. Plast. 82, 283–304.

Hiura, F., 2010. Latent Hardening in Pure Magnesium Single Crystals.

Kabirian, F., Khan, A.S., Gnäupel-Herlod, T., 2015. Visco-plastic modeling of mechanical responses and texture evolution in extruded AZ31 magnesium alloy for various loading conditions. Int. J. Plast. 68, 1–20.

Kalidindi, S.R., 1998. Incorporation of deformation twinning in crystal plasticity models. J. Mech. Phys. Solids 46, 267–271.

Knezevic, M., Levinson, A., Harris, R., Mishra, R.K., Doherty, R.D., Kalidindi, S.R., 2010. Deformation twinning in AZ31: influence on strain hardening and texture evolution. Acta Mater. 58, 6230–6242.

Knezevic, M., McCabe, R.J., Lebensohn, R.A., Tomé, C.N., Liu, C., Lovato, M.L., Mihaila, B., 2013. Integration of self-consistent polycrystal plasticity with dislocation density based hardening laws within an implicit finite element framework: application to low-symmetry metals. J. Mech. Phys. Solids 61, 2034–2046.

Koike, J., Fujiyama, N., Ando, D., Sutou, Y., 2010. Roles of deformation twinning and dislocation slip in the fatigue failure mechanism of AZ31 Mg alloys. Scr. Mater. 63, 747–750.

Kondo, R., Tadano, Y., Shizawa, K., 2014. A phase-field model of twinning and detwinning coupled with dislocation-based crystal plasticity for HCP metals. Comput. Mater. Sci. 95, 672–683.

Kumar, M.A., Kanjarla, A.K., Niezgoda, S.R., Lebensohn, R.A., Tomé, C.N., 2015. Numerical study of the stress state of a deformation twin in magnesium. Acta Mater. 84, 349–358.

Lavrentev, F.F., Pokhil, Y.A., 1975. Relation of dislocation density in different slip systems to work hardening parameters for magnesium crystals. Mater. Sci. Eng. 18, 261–270.

Lebensohn, R.A., Tomé, C.N., 1993. A self-consistent anisotropic approach for the simulation of plastic deformation and texture development of polycrystals: application to zirconium alloys. Acta Metall. Mater. 41, 2611–2624.

Lévesque, J., Mohammadi, M., Mishra, R.K., Inal, K., 2016. An extended Taylor model to simulate localized deformation phenomena in magnesium alloys. Int. J. Plast. 78, 203–222.

Liu, C., Shanthraj, P., Diehl, M., Roters, F., Dong, S., Dong, J., Ding, W., Raabe, D., 2018. An integrated crystal plasticity–phase field model for spatially resolved twin nucleation, propagation, and growth in hexagonal materials. Int. J. Plast. 106, 203–227.

Liu, Y., Wei, Y., 2014. A polycrystal based numerical investigation on the temperature dependence of slip resistance and texture evolution in magnesium alloy AZ31B. Int. J. Plast. 55, 80–93.

Long, T.R., Smith, C.S., 1957. Single-crystal elastic constants of magnesium and magnesium alloys. Acta Metall. 5, 200–207.

Mirza, F.A., Chen, D.L., Li, D.J., Zeng, X.Q., 2013. Low cycle fatigue of a rare-earth containing extruded magnesium alloy. Mater. Sci. Eng. A 575, 65–73.

Mokdad, F., Chen, D.L., 2015. Strain-controlled low cycle fatigue properties of a rare-earth containing ZEK100 magnesium alloy. Mater. Des. 67, 436–447.

Murphy-Leonard, A.D., Pagan, D.C., Beaudoin, A., Miller, M.P., Allison, J.E., 2019. Quantification of cyclic twinning-detwinning behavior during low-cycle fatigue of pure magnesium using high energy X-ray diffraction. Int. J. Fatigue 125, 314–323.

Oppedal, A.L., El Kadiri, H., Tomé, C.N., Kaschner, G.C., Vogel, S.C., Baird, J.C., Horstemeyer, M.F., 2012. Effect of dislocation transmutation on modeling hardening mechanisms by twinning in magnesium. Int. J. Plast. 30–31, 41–61.

Oppedal, A.L., El Kadiri, H., Tomé, C.N., Vogel, S.C., Horstemeyer, M.F., 2013. Anisotropy in hexagonal close-packed structures: improvements to crystal plasticity approaches applied to magnesium alloy. Philos. Mag. 93, 4311–4330.

Ostapovets, A., Molnár, P., Jäger, A., 2013. Visco-plastic self-consistent modelling of a grain boundary misorientation distribution after equal-channel angular pressing in an AZ31 magnesium alloy. J. Mater. Sci. 48, 2123–2134.

Paramatmuni, C., Kanjarla, A.K., 2019. A crystal plasticity FFT based study of deformation twinning, anisotropy and micromechanics in HCP materials: application to AZ31 alloy. Int. J. Plast. 113, 269–290.

Prakash, A., Nöhring, W.G., Lebensohn, R.A., Höppel, H.W., Bitzek, E., 2015. A multiscale simulation framework of the accumulative roll bonding process accounting for texture evolution. Mater. Sci. Eng., A 631, 104–119.

Prasad, N.S., Narasimhan, R., Suwas, S., 2017. Effects of lattice orientation and crack tip constraint on ductile fracture initiation in Mg single crystals. Int. J. Plast. 97, 222–245.

Proust, G., Tomé, C.N., Jain, A., Agnew, S.R., 2009. Modeling the effect of twinning and detwinning during strain-path changes of magnesium alloy AZ31. Int. J. Plast. 25, 861–880.

Proust, G., Tomé, C.N., Kaschner, G.C., 2007. Modeling texture, twinning and hardening evolution during deformation of hexagonal materials. Acta Mater. 55, 2137–2148.

Qiao, H., Agnew, S.R., Wu, P.D., 2015. Modeling twinning and detwinning behavior of Mg alloy ZK60A during monotonic and cyclic loading. Int. J. Plast. 65, 61–84.

Qiao, H., Barnett, M.R., Wu, P.D., 2016. Modeling of twin formation, propagation and growth in a Mg single crystal based on crystal plasticity finite element method. Int. J. Plast. 86, 70–92.

Segurado, J., Lebensohn, R.A., Llorca, J., Tomé, C.N., 2012. Multiscale modeling of plasticity based on embedding the viscoplastic self-consistent formulation in implicit finite elements. Int. J. Plast. 28, 124–140.

Slutsky, L.J., Garland, C.W., 1957. Elastic constants of magnesium from 4.2°K to 300°K. Phys. Rev. 107, 972–976.

Staroselsky, A., Anand, L., 1998. Inelastic deformation of polycrystalline face centered cubic materials by slip and twinning. J. Mech. Phys. Solids 46, 671–673.

Staroselsky, A., Anand, L., 2003. A constitutive model for hcp materials deforming by slip and twinning: application to magnesium alloy AZ31B. Int. J. Plast. 19, 1843–1864.

Tomé, C.N., Lebensohn, R.A., Kocks, U.F., 1991. A model for texture development dominated by deformation twinning: application to zirconium alloys. Acta Metall. Mater. 39, 2667–2680.

Van Houtte, P., 1978. Simulation of the rolling and shear texture of brass by the Taylor theory adapted for mechanical twinning. Acta Metall. 26, 591–604.

Voyiadjis, G.Z., Yaghoobi, M., 2019. Chapter 3 - nonlocal crystal plasticity. In: Voyiadjis, G.Z., Yaghoobi, M. (Eds.), Size Effects in Plasticity. Academic Press, pp. 191–232.

Wang, H., Raeisinia, B., Wu, P.D., Agnew, S.R., Tomé, C.N., 2010. Evaluation of self-consistent polycrystal plasticity models for magnesium alloy AZ31B sheet. Int. J. Solids Struct. 47, 2905–2917.

Wang, H., Wu, P.D., Tomé, C.N., Huang, Y., 2010. A finite strain elastic-viscoplastic self-consistent model for polycrystalline materials. J. Mech. Phys. Solids 58, 594–612.

Wang, H., Wu, P.D., Tomé, C.N., Wang, J., 2012. A constitutive model of twinning and detwinning for hexagonal close packed polycrystals. Mater. Sci. Eng. A 555, 93–98.

Wang, H., Wu, P.D., Wang, J., 2013. Modeling inelastic behavior of magnesium alloys during cyclic loading-unloading. Int. J. Plast. 47, 49–64.

Wang, H., Wu, P.D., Wang, J., Tomé, C.N., 2013. A crystal plasticity model for hexagonal close packed (HCP) crystals including twinning and de-twinning mechanisms. Int. J. Plast. 49, 36–52.

Wu, L., 2009. Mechanical Behavior and the Role of Deformation Twinning in Wrought Magnesium Alloys Investigated Using Neutron and Synchrotron X-Ray Diffraction. Ph.D. Thesis. University of Tennessee, Knoxville.

Wu, L., Agnew, S.R., Brown, D.W., Stoica, G.M., Clausen, B., Jain, A., Fielden, D.E., Liaw, P.K., 2008. Internal stress relaxation and load redistribution during the twinning–detwinning-dominated cyclic deformation of a wrought magnesium alloy, ZK60A. Acta Mater. 56, 3699–3707.

Wu, L., Agnew, S.R., Ren, Y., Brown, D.W., Clausen, B., Stoica, G.M., Wenk, H.R., Liaw, P.K., 2010. The effects of texture and extension twinning on the low-cycle fatigue behavior of a rolled magnesium alloy, AZ31B. Mater. Sci. Eng., A 527, 7057–7067.

Wu, L., Jain, A., Brown, D.W., Stoica, G.M., Agnew, S.R., Clausen, B., Fielden, D.E., Liaw, P.K., 2008. Twinning-detwinning behavior during the strain-controlled low-cycle fatigue testing of a wrought magnesium alloy. ZK60A. Acta Mater. 56, 688–695.

Wu, P.D., Guo, X.Q., Qiao, H., Lloyd, D.J., 2015. A constitutive model of twin nucleation, propagation and growth in magnesium crystals. Mater. Sci. Eng., A 625, 140–145.

Wu, W., Lee, S.Y., Paradowska, A.M., Gao, Y., Liaw, P.K., 2012. Twinning–detwinning behavior during fatigue-crack propagation in a wrought magnesium alloy AZ31B. Mater. Sci. Eng., A 556, 278–286.

Yaghoobi, M., Ganesan, S., Sundar, S., Lakshmanan, A., Rudraraju, S., Allison, J.E., Sundararaghavan, V., 2019. PRISMS-Plasticity: an open-source crystal plasticity finite element software. Comput. Mater. Sci. 169, 109078.

Yu, Q., Jiang, Y., Wang, J., 2015. Cyclic deformation and fatigue damage in single-crystal magnesium under fully reversed strain-controlled tension-compression in the [1010] direction. Scr. Mater. 96, 41–44.

Yu, Q., Zhang, J., Jiang, Y., 2011. Fatigue damage development in pure polycrystalline magnesium under cyclic tension-compression loading. Mater. Sci. Eng. A 528, 7816–7826.

Zhang, H., Jérusalema, A., Salvati, E., Papadaki, C., Fong, K.S., Song, X., Korsunsky, A.M., 2019. Multi-scale mechanisms of twinning-detwinning in magnesium alloy AZ31B simulated by crystal plasticity modeling and validated via in situ synchrotron XRD and in situ SEM-EBSD. Int. J. Plast. 119, 43–56.

Zhang, J., Joshi, S.P., 2012. Phenomenological crystal plasticity modeling and detailed micromechanical investigations of pure magnesium. J. Mech. Phys. Solids 60, 945–972.

Zhang, J., Yu, Q., Jiang, Y., Li, Q., 2011. An experimental study of cyclic deformation of extruded AZ61A magnesium alloy. Int. J. Plast. 27, 768–787.